SURFACE ENHANCED RAMAN SPECTROSCOPY FOR BACTERIA DETECTION

MAHAMAYA DEB

Thesis submitted to the University of Ottawa
Faculty of Graduate and Postdoctoral Studies
in partial fulfillment of the requirements for
the Master of Applied Science (M.A.Sc) degree in
Electrical and Computer Engineering

Ottawa-Carleton Institute for Electrical and Computer Engineering
School of Electrical Engineering and Computer Science
Faculty of Engineering
University of Ottawa

Abstract

This thesis focuses on the optimization of surface enhanced Raman for bacteria detection. Many factors influence the outgoing Raman signal in SERS. Coating the nanoparticles used in SERS with a capping agent is one way to enhance the Raman signal. Capping agents can play a significant role in the interaction between the nanoparticles and the bacteria, in turn contributing to the detection of pathogens. To understand the potential of optimizing the capping agent for gold nanoparticles in SERS detection of bacteria, three capping agents — thioglucose (which was not applied previously for the SERS analysis of bacteria), polyvinylpyrrolidone (PVP), and citrate — were tested for their ability to improve species identification and Staphylococcus aureus strain discrimination. The generated samples were run under a dark-field microscopy integrated SERS setup. Upon discriminant analysis, the collected dataset showed that thioglucose and citrate performed well in species identification. However, thioglucose performed better than citrate and PVP in strain discrimination because of its strong ability to integrate with nucleic acid components inside the bacteria cells.

The second experiment explored if SERS can be used to diagnose periprosthetic joint infections (PJI) in shoulder tissue sample. Since the application of SERS on tissue for diagnostic purposes is novel, both ex-situ and in-situ gold nanoparticles were tested. For the in-situ gold nanoparticle integration into tissue samples, the UV reduction method was applied on the samples to generate gold nanoparticles inside the tissues. Multiple conditions were applied on the tissue samples controlling the UV power and UV exposure time. The samples were run in the same dark-field integrated Raman setup initially. The collected data showed that the in-situ gold nanoparticle integration into the shoulder tissue samples through the UV reduction

method was successful and has potential. However, the optimum SERS condition could not be confirmed from this analysis due to the high variation of the Raman signal from one tissue sample to the other which generated inconsistent results even in the same applied condition. This suggested that distribution of gold nanoparticle integrated to the tissue was uneven, and thus affected the consistency of the outcomes from the process. Dark field SERS setup was then modified, and a scanning microscope part was incorporated to the system. Rigorous analysis of the SERS spectra from the scanned image and the Raman band assignment of these spectra showed that region high in collagen and protein can provide strong SERS signal. Therefore, to decide on the optimum SERS condition for PJI diagnosis by SERS, scanned image spectra from samples should be obtained. The comparison of all averaged spectra calculated from the highest Raman integral spectra acquired for each condition can point out to the optimum SERS condition. Besides, the relevant band assignment of each spectrum can provide information to understand the mechanism of SERS on shoulder tissue samples.

Acknowledgements

I would like to thank all individuals from whom I have received immense support and guidance during this period of my research. During this time, I have met many great personalities and learned a lot from them. I would like to thank all those people with whom I got opportunities to work during my studies at the University of Ottawa.

First, I would like to convey my sincere gratitude to my supervisor Professor Hanan Anis for her support, guidance, and willingness to listen to my ideas. I am exceptionally fortunate to be receiving such good guidance and mentoring during my research. Her extensive knowledge in various fields allows her to guide research students in the correct track to accomplish their goals.

I would also like to thank PhD candidate Robert Hunter for his enormous time and support in guiding me during my research. His timely advice and scientific scrutiny helped me to accomplish the tasks in a proper manner. His suggestions and feedback always enriched my knowledge in the field of biophotonics.

The work presented in this thesis was done in close collaboration with other research teams and laboratories. I would like to express my sincere thanks to all of them for providing the materials, guidance, and research facilities I needed to fulfill my research goals.

Next, I would like to express my gratitude to all the members of Hanan Anis's research group. Their beneficial suggestions and ideas helped me proceed well during my research. I am thankful to be a part of this group and have the opportunity to work with all these nice people as my colleagues.

My research work has been possible for the blessings and support I received from my family. I would like to thank my parents, who always trusted and blessed me for

the best of my future. I would also like to thank my husband Robi Kormokar, who was always beside me to encourage and showed me the required steps to move forward during my research. Without his immense support, I would not have finished my research.

Lastly, I recognize that this research would not have been possible without the assistance from the financial agencies that support my research group and the School of Electrical Engineering and Computer Science, Graduate Studies, at the University of Ottawa. I am grateful to all of them for the support.

Table of Contents

List of Figures

List of Tables

Glossary

airPLS: adaptive iteratively reweighted Penalized Least Squares

BP: Band Pass

CAMaR: Center for Advanced Material Research

CCD: Charge Coupled Device

CMOS: Complementary Metal Oxide Semiconductor

DFA: Dark-Field Aperture

DLS: Dynamic Light Scattering

DNA: Deoxyribonucleic Acid

EDL: Electric Double Layer

GA-SVM: Genetic Algorithm Support Vector Machine

LB: Lysogeny Broth

LSPR: Localized Surface Plasmon Resonance

MALDI-TOF: Matrix-Assisted Laser Desorption Ionization Time-Of-Flight

MATLAB: Matrix Laboratory

MRSA: Methicillin-Resistive Staphylococcus aureus

MSSA: Methicillin-Sensitive Staphylococcus aureus

NA: Numerical Aperture

NF: Notch Filter

NIR: Near Infrared Range

PCR: Polymerase Chain Reaction

PLS: Partial Least Square

PJI: Periprosthetic Joint Infection

PVP: Polyvinylpyrrolidone

R6G: Rhodamine 6G

RNA: Ribonucleic Acid

RQK: Rational Quadratic Kernel

SERS: Surface Enhanced Raman Spectroscopy

SEM: Scanning Electron Microscope

SNR: Signal to Noise Ratio

SP-DCM: Short Pass Dichroic Mirror

TG: Thioglucose

Chapter 1 Thesis objectives and contributions

This chapter includes the thesis objectives and contributions to this area of study, as well as my personal contributions to the research work.

1.1 Objective

The prevalence of hospital acquired infections and antibiotic resistant pathogens necessitates the development of bacteria sensing systems that do not require sample amplification via conventional cell culturing, which can be prohibitively time-consuming and can result in many health complications. Surface-enhanced Raman spectroscopy (SERS) is a technique that can be applied to develop fast screening systems for bacterial presence in biological samples.

Our group has developed a SERS based platform for bacteria detection using nanoparticles, hollow core fibers, microfluidics and machine learning [1]. This thesis builds on this work and explores two issues. The first is the optimization of capping agents of gold nanoparticles for SERS detection of bacteria. Optimizing the capping agents in nanoparticle synthesis is important because capping agents are responsible for controlling the morphological features and chemical properties of the nanoparticles that are essential for SERS. Second, the thesis explores the use of both in-situ and ex-situ nanoparticles to achieve maximum enhancement of SERS for shoulder tissue samples acquired from synovial biopsy. Application of in-situ and ex-situ nanoparticles in shoulder tissue samples can potentially enhance the ability of SERS to identify pathogens responsible for prosthetic joint infection (PJI) in patients after shoulder replacement surgery.

1.2 Contributions

The research work done for this thesis will result in two journal articles. The first part of the work resulted into a paper "Rapid detection of bacteria using gold nanoparticles in SERS with three different capping agents: thioglucose, polyvinylpyrrolidone, and citrate," which has been published to the journal Spectrochimica Acta Part A: Molecular and Biomolecular Spectroscopy. The second part of this thesis work contains the study on the application of SERS technique on shoulder tissue and it is still ongoing.

1.3 Thesis outline

This thesis is organized as follows.

Chapter 2 first introduces Raman spectroscopy and its limitations. Then it defines surface-enhanced Raman spectroscopy (SERS) and discusses the mechanism behind this phenomenon along with different factors that influence its outcome. Finally, it describes two types of SERS configurations, intrinsic and extrinsic, to provide a vivid picture of SERS techniques and introduces In-situ and Ex-situ SERS.

Chapter 3 discusses the first research work carried out for this thesis: the optimization of capping agents on gold nanoparticles for the SERS detection of bacteria. This chapter describes the capping agents chosen for this experiment and their synthesis with gold nanoparticles used for this research, followed by the characterization of generated gold nanoparticles. The experimental setup and the method of sample preparation for the application of SERS on bacteria are then described. The final two subsections of this chapter include the results and a discussion of their interpretation.

Chapter 4 explores the application of SERS on shoulder tissue. First, the chapter explains periprosthetic joint infection and the potential for using SERS to improve diagnosis. The following sections describe the experimental setup used, the different steps of sample preparation done for applying different conditions on multiple sets of tissue slides, and the data analysis approach. The chapter ends with a discussion of the results and their interpretation.

Chapter 5 summarizes the research and suggests future work based on the two experimental studies discussed in this thesis.

Chapter 2 Raman spectroscopy and surface-enhanced Raman spectroscopy (SERS)

2.1 Introduction

Raman spectroscopy is a technique based on vibrational spectroscopy [2] that obtains information on the structural and chemical properties of molecules by quantifying the frequency shift from molecular transition states. Inelastic scattering of photons is observed when photons with sufficient energy are incident on target molecules and excite the molecules to a higher state, and energy is released in scattered photons to return to lower energy states. This phenomenon, known as Raman effect, was discovered by C. V. Raman and reported in 1928 [3]. The first Raman spectra were collected by Raman in a spectroscope designed with a prism and a photographic plate, and the samples in a spherical flask were excited by a mercury arc lamp [4]. This kind of spontaneous Raman scattering process produces very weak Raman signals, but the development of lasers greatly improved the applications and analysis prospects of Raman spectroscopy. Targeting samples with incident laser beams can produce highly efficient and observable stimulated Raman scattering [5]. This chapter discusses the theory and limitations of Raman spectroscopy. It then focuses on surface-enhanced Raman spectroscopy (SERS) and its mechanism, including the factors that influence the enhancement effect in SERS.

2.2 Theory of Raman spectroscopy

When a sample is illuminated in general circumstances with an incident light of frequency $\vartheta_{\circ}$, then the spectrum of the scattered light can be obtained from the Rayleigh scattering and Raman scattering (Figure 2.1) [5]. As the Raman scattering

is inelastic, the Raman-scattered light beam contains components of different frequencies for the transition of photons to different electronic states. The components of the scattered signal with lower frequencies than the incident frequency are known as Stokes components, and the components of the scattered signal with higher frequencies are known as anti-Stokes components (Figure 2.1 and 2.2) [5].

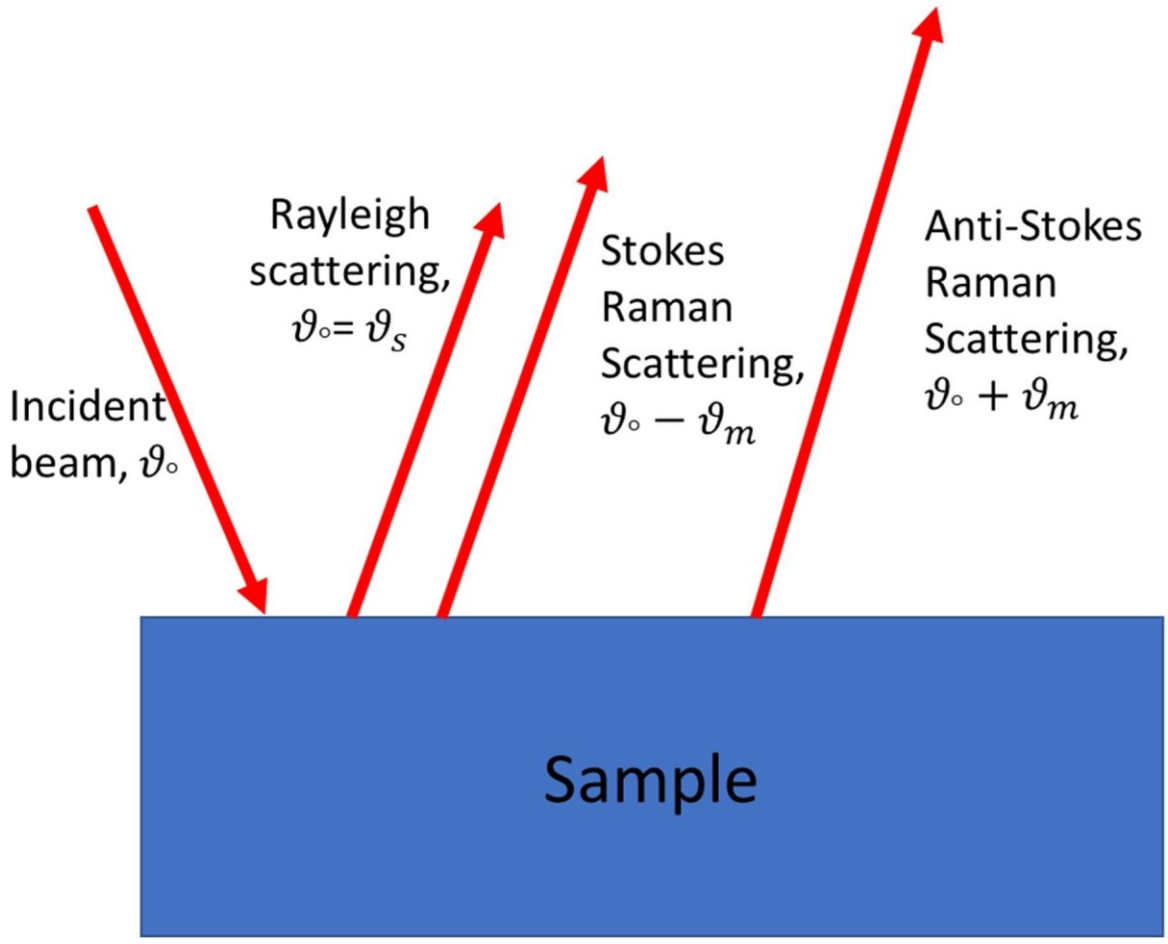

Figure 2.1: Light scattering from a sample illuminated by an incident beam [5].

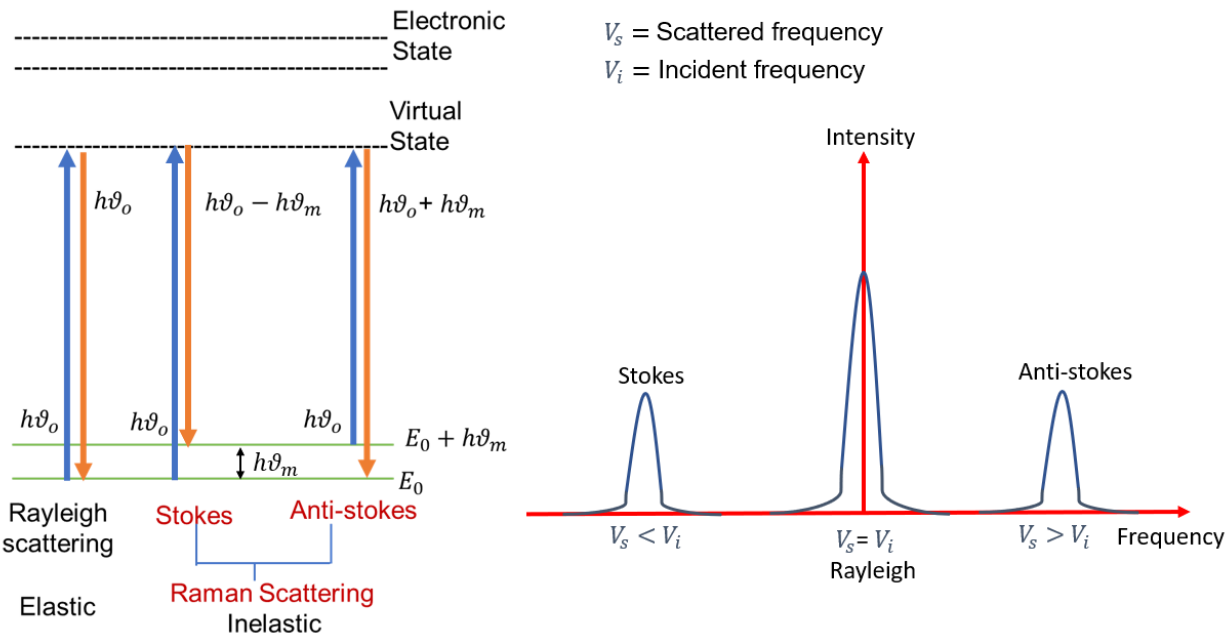

Figure 2.2: Schematic diagram to show transition states in scattering process and the Raman spectrum [5].

The lost or gained amount of energy in the inelastic scattering process by a photon is called Raman shift and is calculated as [6]

$$\Delta E_R = E_I - E_S \quad (1)$$

Here, E_I = incident photon energy

E_S = scattered photon energy

Let us consider the energy of an incident photon is $h\vartheta_\circ$; the ground state is E$_\circ$ and the difference of energy between the ground state and the transition state is $h\vartheta_m$ as shown in the Figure 2.2. Then from equation (1), for the Stokes components, Raman shift $\Delta E = h\vartheta_\circ - h\vartheta_m$, and for the anti-Stokes components, Raman shift $\Delta E = h\vartheta_\circ + h\vartheta_m$. Raman shifts are expressed in wavenumbers with the usual unit of cm^{-1} .

Raman peaks in the Raman spectrum are generated from the vibrational modes of the target molecule, and the corresponding Raman shift of the peaks are equivalent to the vibrational energy of the modes [6]. Not all vibrational modes can produce strong Raman scattered signal, and the Raman selection rule can be explained by the interaction of bonds with the electromagnetic radiation. When a molecule is excited by an electric field E, the bonds in the molecule vibrates. Bond polarizability α is induced from this periodic change of the bond length and α is associated with the dipole moment P induced in the molecule by the incident electric field, E as given by [7]

$$P = \alpha E \tag{2}$$

Here, α denotes the polarizability of the molecule. The amount of distortion of the electron cloud surrounding a molecule is observed from the polarizability. The change in the parameter P induces Raman scattering; therefore, the intensity of the Raman scattered signal is the square of the induced dipole moment [8]

$$I_{Raman} \propto \alpha^2 \, E^2 \tag{3}$$

2.3 Limitations of Raman spectroscopy and solution

Generally, a Raman scattered signal is very weak, and the molecules applied in the process thus give low Raman efficiency. Consequently, it is hard to work with low concentrations and small quantities of samples using Raman spectroscopy. From equation (3), it is known that the intensity of Raman spectrum depends on the polarizability and the incident electric field. If both parameters are increased, then the intensity of the scattered Raman signal should increase, and so the Raman efficiency should increase even for low concentrations of samples.

2.4 Surface-enhanced Raman spectroscopy

When analyte molecules are attached to metal substrates or nanoparticles and a laser beam is incident on the analyte molecules in this condition, then stronger Raman scattered signals are generated from the analyte molecules due to the plasmon resonance effect of the metal interacting with the analyte molecules. This phenomenon is known as surface-enhanced Raman scattering (SERS) (Figure 2.3). The enhancement of the Raman scattered signal in this approach occurs when the metal nanostructure is in localized surface plasmon resonance (LSPR) mode [9]. Metals show this phenomenon for their unique optical properties that arise primarily from the free electrons in the conduction band [9]. The enhancement in the SERS signal is generated when the metallic nanostructures are excited optically due to multiple elements which are- the increase in local resonant electromagnetic field intensity, the Purcell effect, charge transfer resonances and molecular resonances [9]. These elements contributing to Raman signal enhancement are dependant on the size, shape and materials of the nanostructures [9, 10]. Any variation in the size, shape of the metallic substrates in the SERS can change their plasmonic activity and the spectral position [6, 10]. The extinction spectrum of the metallic nanostructures is wavelength dependent, and it effects the excitation wavelength to apply in SERS. To achieve the largest SERS enhancement, the incident laser wavelength in SERS is required to be close to the surface plasmon resonance wavelength of the metallic nanostructure [6]. This effect was first reported by Fleischmann et al. in 1974 when they observed the phenomena from pyridine adsorbed to silver electrodes roughened electro-chemically [11].

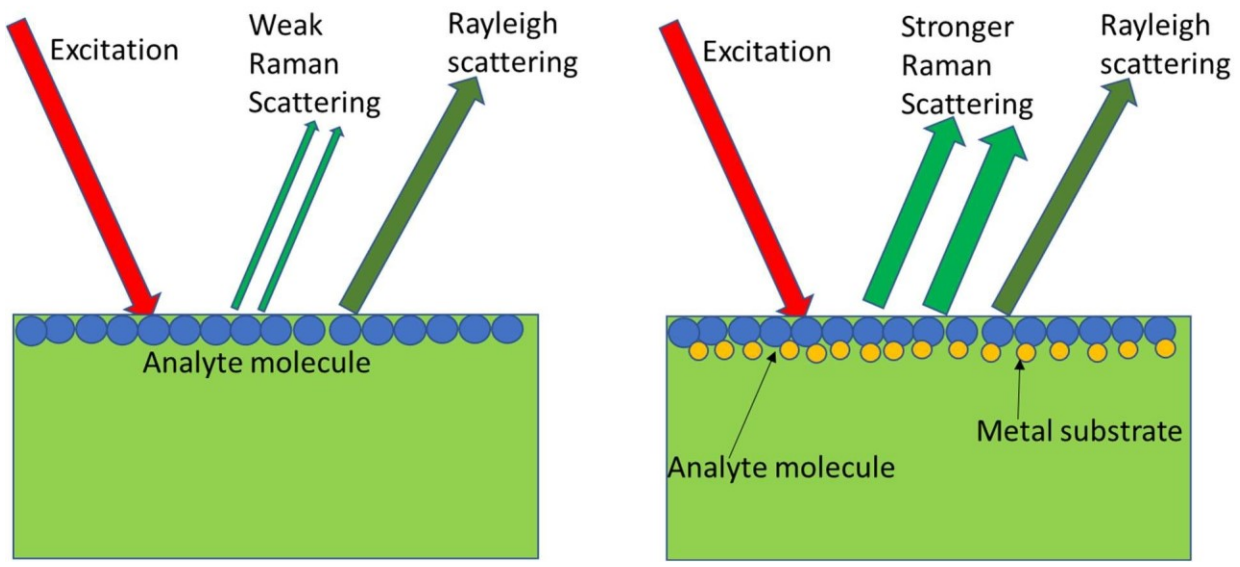

Figure 2.3: Surface-enhanced Raman scattering [6].

The enhancement in Raman intensity by SERS helps to increase the intensity of the Raman scattered signal and overcome the limitations of normal Raman spectroscopy. The maximum SERS enhancement can be achieved from analyte molecules attached to hotspots on the surface of the metal particles. For spherical nanoparticles, the maximum enhancement factor is in the order of $\sim 10^6$ [6]. Besides, the material of metal substrates or metal nanoparticles may vary based on the application. For instance, in SERS detection of bacteria, gold nanoparticles are preferred because of its less reactivity and low toxicity to the bacteria cells [12].

Excitation wavelength is also an important factor to consider in SERS. An optimum excitation wavelength of the incident beam on the SERS substrate attached to the analyte molecules is necessary to produce maximum enhanced Raman signal from the molecules [6]. Good enhancement is observed from a SERS substrate in a limited excitation wavelength range. Most SERS substrates provide good enhancement in the visible or near infrared excitation wavelength and it is a typical range of operation for experiments with molecular Raman scattering [6].

Two main theories are considered the basics in explaining the effect of SERS: electromagnetic theory and chemical theory [6]. Electric field enhancement through strong interactions of analyte molecules with the surface plasmon resonance was first proposed by Jeanmaire and Van Duyne [13]. Chemical enhancement from the interaction between a molecule and the metal surface was suggested by Albrecht and Creighton [14]. Since the early 1980s, research on SERS and its mechanism has developed in the fields of chemistry, physics, and engineering. In this thesis, only the electromagnetic theory is discussed in the next section, as it is considered to contribute most of the SERS enhancement, producing as high as $\sim 10^{14}$ fold enhancement through the surface plasmons' excitation in metal nanostructures [6, 15, 16].

2.5 Mechanism of SERS

SERS enhancement occurs in two steps [8]. Primary enhancement occurs due to the localized surface plasmon resonance (LSPR) of the SERS substrate. Collective oscillations of conduction electrons on the nanosphere are known as surface plasmons; as these surface plasmons are excited, enhancement of the local field can be experienced by an adsorbed molecule [17]. When a SERS substrate is excited by a laser beam of optimum wavelength, the localized electric field of the molecule enhances as shown in the equation (4)

$$E_{loc} = M_{loc}(\lambda_{\circ}).\, E_{\circ} \tag{4}$$

Here the enhancement factor is $M_{loc}(\lambda_{\circ})$ at the incident wavelength $\lambda_{\circ}$. The stronger localized electric field then produces an oscillating dipole at Raman scattered wavelength (λ_R) and radiates. The overall SERS intensity then can be written as

$$I_{SERS} = [M(\lambda_R).\ M(\lambda_\circ)]\ .\alpha^2 E^2 \quad (5)$$

$$I_{SERS} = [M(\lambda_R).\ M(\lambda_\circ)]\ .I_{Raman} \quad (6)$$

If the frequency of the Raman scattered signal is close to the incident beam, then the equation (6) can be written as

$$I_{SERS} \approx [M(\lambda^\circ)]^4.\ I_{Raman} \quad (7)$$

The approximation in equation (7) shows the overall trend theoretically with the SERS phenomenon that the process can generate stronger Raman signal than normal Raman spectroscopy generates. This allows SERS to be a sensitive tool even at low sample molecule concentration. Moreover, it can act efficiently as a vibrational fingerprint in molecular detection.

2.6 Factors affecting SERS

SERS technique is now applied to rapidly detect and quantify biomolecules and other substances. This application is possible because of the enhancement in the Raman scattered signal from target molecules in SERS. Enhancement of the scattered signal is controlled by factors that can be adjusted in the process to achieve the best outcome. The three main factors that influence SERS results are the choice of metallic nanoparticles, the choice of incident wavelength and the treatment of the SERS target molecule.

'SERS substrates' generally mean any metallic nanostructures that can produce SERS enhancement. These nanostructures can be either fabricated or synthesised in colloid solution. Colloid solutions of the metallic nanoparticles are considered the simplest way to integrate SERS in a system [6]. Silver is used for many SERS applications due to its strong plasmonic properties. However, silver is toxic for

bacteria cells [12]. So, in biomolecule detection by SERS, gold is preferred to silver, especially because the optical absorption of gold is comparable to that of silver at wavelengths longer than 600 nm [6]. This shows that the selection of appropriate metallic nanoparticles for a particular SERS application is important in order to obtain the maximum SERS response. Maximum enhancement in SERS response can lead to an efficient qualitative and quantitative analysis of the sample biomolecule or bio-cell. Figure 2.4 shows the citrate capped gold nanoparticles solution.

Figure 2.4: Colloidal solution of gold nanoparticles.

Besides the material selection of the nanoparticles, their size and shape can play a significant role in SERS enhancement based on the SERS application. In general SERS signal enhancement depends on the optimum size of the nanoparticles. Regardless of the exact size of the nanoparticles for optimum SERS enhancement, one can consider the effective SERS range [18]. If the particles are too small, the effective conductivity and light scattering properties decrease which are required for the SERS enhancement [18]. With the increment of particle size, the SERS effect

increases as the electron number increases. If the particle size increases to such level where the size is comparable to the excitation wavelength, then the particles get excited to nonradiative modes which then reduces SERS effect [18]. Different shaped nanoparticles can be generated by adding different surfactants in the synthesis process [9]. They can be spherical, star, cube, rod and of many more shapes. However, selection of proper shape to produce maximum SERS enhancement is important. Based on the shape of the nanoparticle's, large diversity in the plasmon resonances can be observed. For instance, in the case of ellipsoid shaped nanoparticles, localization enhancement from the pointy ends can be observed [6]. Therefore, additional LSPR effects can evolve with the change of shape. Strong red shifts can be generated by some of these which can largely enhance the local fields [6]. However, the shape should be selected based on the application purpose and the size, shape of the target molecules. It is observed that for reasonable SERS enhancement, the distance between SERS surface and the target molecule needs to be within (1-30) nm [18].

SERS enhancement is strongly dependent on the excitation wavelength [6]. For specific material, loss of energy due to extinction is maximized at the maximum absorption wavelength. This wavelength can be calculated from the extinction spectrum of the material. For SERS application, the incident wavelength must be at a window range that allows maximum enhancement with minimum extinction. Pilot et al. describe the three window ranges for the incident wavelengths that generally allow minimum extinction [19]: (a) between 650 and 950 nm (NIRI), (b) between 1000 and 1350 nm (NIR-II), and (c) between 1500 and 1800 nm (NIR-III). For biomedical applications, the first range (from 650 to 950 nm) is applied to allow for propagation of the incident light through the tissue. Moreover, shorter excitation

wavelengths in the window range increase the Raman cross section [19], thereby enhancing the Raman signal.

Raman scattered signal amplification can vary depending on the combination of the target molecule and the substrate used to enhance the SERS signal. Therefore, optimization of the SERS process depends on the target molecule and the objective of the particular SERS application. The target molecule's surface area, structure, and chemical composition are all important parameters to take into account because they can allow strong adsorption of the nanoparticles on the target molecule surface.

2.7 SERS configuration

For biosensing applications, SERS can be configured in either of two main methods: intrinsic SERS and extrinsic SERS. These two methods are discussed in the following sub-sections.

2.7.1 Intrinsic SERS

When an analyte molecule is directly applied on the nanostructure and the generated Raman spectrum from the specimen is collected to identify the molecule, then this method is called intrinsic SERS (as seen in Figure 2.5) [20]. To design a SERS detection system with high specificity, suitable antibodies, aptamers, or other related molecules that bind well with the target molecule can also be attached or fabricated on the nanostructure. This helps in capturing the specific target molecule. Comparing the Raman spectra from before and after the capture of the molecule contributes to species identification [20]. Intrinsic SERS is preferred in detecting macro-sized biomolecules and qualitatively analyzing them. This method provides structural information about the target molecule, expediting the qualitative analysis of similar kinds of samples [18]. Intrinsic SERS can facilitate inherent multiplexing by

multivariate analysis leveraging unique spectral components between samples. However, in intrinsic SERS, molecules can give a vague response if the molecule is insensitive in Raman shift and low in concentration [18]. A single type of nanoparticle with high affinity for bacteria can provide intrinsic spectrum that can facilitate multiplexed sensor at low cost for diagnosis purpose. For this reason, intrinsic method of SERS is applied in optimization of capping agents for SERS detection of bacteria which is presented in Chapter 3 of this thesis.

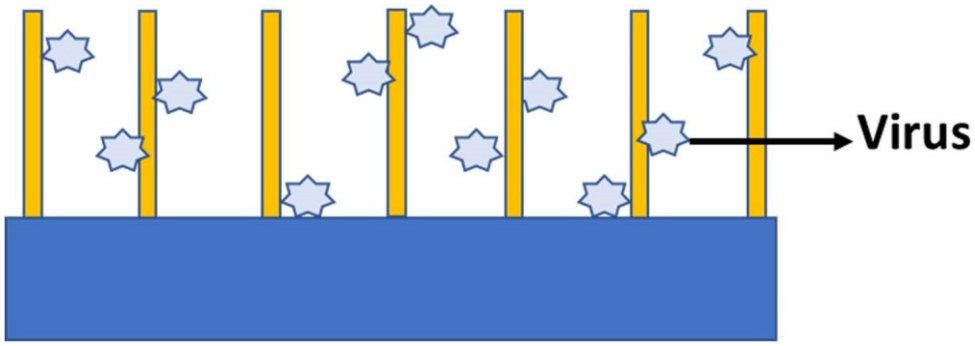

Figure 2.5: Schematic diagram for intrinsic SERS.

2.7.2 Extrinsic SERS

Extrinsic SERS allow Raman reporters to measure the SERS effect from the target molecules. Raman reporters are the molecules that inherit strong Raman active modes [18]. Rotational or vibrational motion of molecules that can induce change in polarizability of the molecule are known as Raman active modes. The modes which cannot induce change in polarizability are not considered Raman active and they do not appear in the Raman spectrum. Common example of Raman reporter is the Raman dyes (e.g. malachite green, methylene blue) that can provide intense Raman signal. Raman reporters are immobilized on the surface of the SERS substrate and then fully enclosed with a protective layer of dielectrics. The protective layer prevents aggregation of nanoparticles and detachment of the Raman reporters for steric hindrance or charge neutralization [18]. This dielectric layer thickness has no

effect on SERS because the reporters are bound to the gold particle directly. However, the distance between SERS surface and the target molecule needs to be within (1-30) nm for the optimum response in SERS [18]. Finally, they are coated with corresponding ligands or antibodies to functionalize the nanoparticles and capture the target molecules. Specificity of the SERS signal in the bacterial detection by extrinsic SERS comes from the attached ligand or antibody. This type of sandwich structure of nanoparticles in extrinsic SERS (as shown in Figure 2.6) is applied in most of the cases where intrinsic SERS fails. Extrinsic SERS is applied successfully for in-vivo SERS imaging of unique and rare cancer cells [1]. However, instrumentation design for extrinsic SERS can be costly whereas low-cost solution is more suitable for global diagnostic purposes [21].

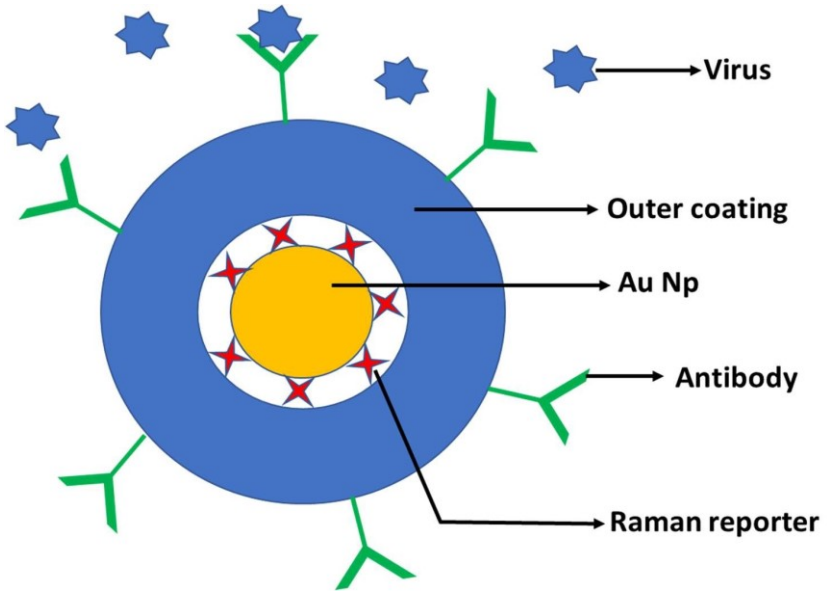

Figure 2.6: Schematic diagram for extrinsic SERS.

Figures 2.5 and 2.6 are presented as an illustrative figure to demonstrate the intrinsic SERS approach. In reality, the size of the nanoparticles is approximately 40nm and the size of the bacteria is (1-5) micrometers. Much better understanding can be gained on the ratio of the sizes of the nanoparticles from the SEM image of the *C.acne* with citrate capped gold nanoparticles as shown in the Figure 2.7.

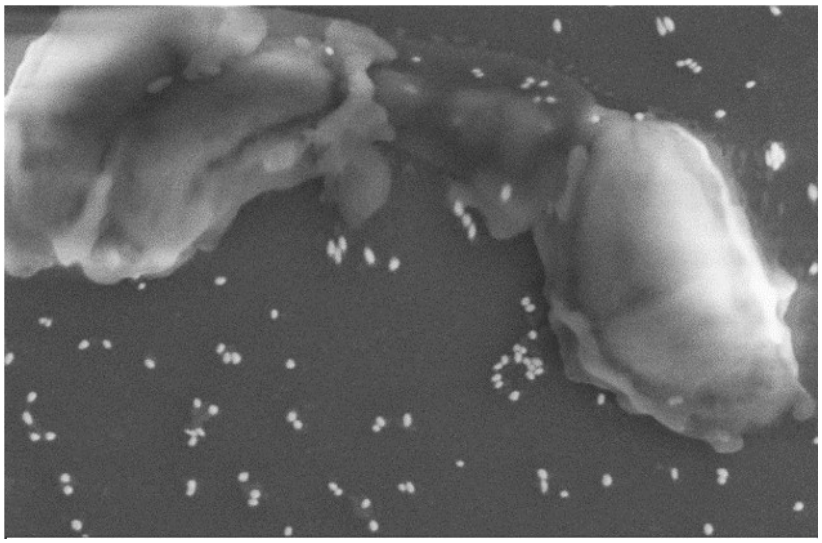

Figure 2.7: *C.acne* with citrate capped gold nanoparticles

2.7.3 In-situ and Ex-situ SERS

Two types of SERS approaches can be used- in-situ SERS and ex-situ SERS. In the ex-situ method, pre-synthesised colloidal nanoparticle solution is added directly to the sample and in the in-situ method, nanoparticles are generated in the sample itself adding the precursor solution to the sample. Both of these approaches are applied in the study of shoulder tissue and presented in Chapter 4.

2.8 Conclusion

SERS is an evolving technique in the detection and identification of biomolecules. There are multiple factors that influence the enhanced Raman signal from the target molecule. Characterizing those factors prior to application of SERS on a selected sample enables the generation of the strongest SERS signal. Moreover, suitable selection of SERS configuration is another influential element for the SERS outcomes.

Chapter 3 Optimization of capping agents on gold nanoparticles for SERS detection of bacteria

3.1 Introduction

Bacterial infections in the human body are increasing at an alarming rate around the world. A significant challenge when diagnosing any kind of microorganisms is the detection time. Given that bacterial loads in clinical samples are generally low, samples require technical sample preparation, culturing, and bacterial isolation prior to detection, all of which delay diagnosis and treatment [22]. Several methods are applied in different clinical settings to diagnose infections. However, they all have some limitations. For example, one of the conventional methods is assay plating, which requires cell culture that can take several days before colony formation can be confirmed [23]. Polymerase chain reaction (PCR) is a molecular-based detection technique that involves DNA amplification. Although the PCR technique works well for mixed samples, it has the potential to give false-positive or false-negative outcomes as a result of contamination from reagents or from carryover products of the reactions that affect the DNA amplification [24]. Another technique is matrix-assisted laser desorption ionization time-of-flight (MALDI-TOF) spectrometry, although it is rarely used in clinical practice [25, 26].

Surface-enhanced Raman spectroscopy (SERS) is an evolving technique for rapid detection of microorganisms that can resolve many of the limitations of conventional methods by exposing the target molecule to nanoparticles and collecting the enhanced Raman scattered signals from the target specimen itself for qualitative and quantitative analysis [1]. In this method, nanometallic structures enhance the inelastic scattered signal from the vibrational modes of targeted molecules through

plasmon resonances [6]. Signal enhancement in SERS depends on the size, shape, and surface functionality of the nanoparticles, as discussed in the previous chapter. Thus, the selection of an appropriate capping agent in SERS is essential to obtaining quality spectra. Optimizing the detection method with other capping agents therefore has the potential to increase the interaction of the nanoparticles with bacteria, eventually improving the diagnosis of these bacteria. This chapter includes details about the experiment run to optimize the capping agent for SERS detection of bacteria, as well as the analytical discussion of the results obtained in the experiment.

3.2 Capping agents used for gold nanoparticles

Usually, nanostructures of plasmonic materials such as gold and silver are used to create SERS substrates. However, gold is more stable than silver because it has lower reactivity and affinity to be oxidized and induces less toxicity in bacteria cells compared to silver [12, 27]. For this reason, the experiments described in this thesis are carried out with gold nanoparticles.

Enhancing the SERS signal depends on the size, shape, and surface functionality of the nanoparticles. Surfactant molecules, or capping agents, influence the morphological features of the nanoparticles and render stability [28] when applied to cover the nanoparticles. These molecules contribute to the chemical interactions between metal nanoparticles and target molecules. For instance, their charge and hydrophobicity determine the interaction of nanoparticles with the lipids and proteins of micro living cells [29, 30]. Thus, the selection of an appropriate capping agent in SERS is essential to obtaining quality spectra. Optimizing the detection method with other capping agents therefore has the potential to increase the interaction of the nanoparticles with bacteria, eventually improving the diagnosis of these bacteria.

Generally, citrate-capped nanoparticles are used for SERS detection of bacteria [12]. Polyvinylpyrrolidone (PVP) is a good surface stabilizer for nanoparticles, and PVP capped gold nanoparticles hinder bacteria growth more than citrate-capped gold nanoparticles do, as found experimentally [31]. Thioglucose (TG) is also a good surface stabilizer for silver or gold nanoparticles that has shown antibacterial activity for antibiotic-resistant strains of bacteria [32]. It is hypothesized that choosing capping agents with good antibacterial properties can contribute to improved SERS detection of bacteria. For this research work, polyvinylpyrrolidone (PVP) was selected along with thioglucose to compare with citrate in the detection of bacteria species and strains.

3.3 Synthesis of gold nanoparticles

Gold (III) chloride powder, sodium citrate, polyvinylpyrrolidone (PVP), 1-β-Thio-D-glucose, sodium, and rhodamine 6G (R6G) were all purchased from Sigma Aldrich. The protocols used in the nanoparticle's synthesis are already established and well-documented. The citrate capped gold nanoparticles are synthesised by the Turkevich method [33]. The PVP capped gold nanoparticles are generated by the ligand displacement approach by displacing citrate from citrate capped gold nanoparticles [34]. Same approach was applied for thioglucose capped gold nanoparticles, and it was successful as confirmed with Raman band assignment of the SERS spectra from each type of gold nanoparticles in the section 3.8.

First, 40 mL of water was mixed with 262 µL of 38 mM gold solution in a 50 mL flask that was heated in a water bath placed on Fisherbrand™ Isotemp™ hot plate stirrer that was set to 200 degrees Celsius for 1 hour, stirring at 700 rpm. After 1 hour, the temperature was reduced to 120℃.

To cap the particle with citrate, 242 μL of 30 mM sodium citrate solution was added to the gold solution and left in the hot water bath for another 30 minutes, stirring at 700 rpm. Within the next hour, a ruby-red colloid solution was obtained, which was the desired outcome for a citrate-capped gold nanoparticle solution.

For the PVP-capped and TG-capped gold nanoparticles, citrate-capped gold nanoparticles were made in the same process, and then PVP or TG was added to a final concentration of 130 mg/L or 6 mM respectively, where it replaced the citrate on the gold nanoparticles, to produce PVP- or TG-capped gold nanoparticles.

3.4 Characterization of gold nanoparticles

The different types of gold nanoparticles were analyzed using UV-vis absorption spectroscopy, dynamic light scattering (DLS), and zeta potential measurements. DLS and zeta potential measurements were obtained from a ZetaSizer instrument from Malvern Panalytical which is a common tool available in the Center for Advanced Material Research (CAMaR) lab facilities and it is calibrated based on standards available in Malvern. For this process, gold nanoparticle solutions were diluted 10^4 fold in degassed, deionized water.

Zeta potential and DLS measurements of the gold nanoparticles were obtained along with the application of UV-Vis spectroscopy to characterize the three differently capped-gold nanoparticles. Information on the net charge of the particles in an environment of liquid is obtained from the zeta potential measurements [35]. Suspension stability and information on the particle coating can be studied well from the zeta potential measurement [35]. When a nanoparticle is solvated in a liquid, electric double layer (EDL) is formed. The EDL consists of two layers: (1) Stern layer and (2) diffuse layer. The diffuse layer has an interface which separates the mobile and immobile ions in the liquid. This interface is termed as the slipping plane

and the electric potential at this plane is called the zeta potential [35]. Zeta potential measurement of the nanoparticles, either positive or negative refers the short term and long term stability of the particles. High zeta potential value shows the good electrical stability whereas low zeta potential shows higher electrical instability which can lead to coagulation or flocculation of the nanoparticles (physical instability) [36]. The zeta potential measurements of the nanoparticles capped with citrate, PVP, and TG were respectively -30.02 mV, -37.5 mV and -6.87 mV. The zeta potential measurements showed that the PVP-capped nanoparticles were more negatively charged in comparison to the citrate-capped and TG-capped gold nanoparticles. Another important analytical tool for characterizing nanoparticle is the dynamic light scattering (DLS). Low cost and easy operation of the tool makes it a primary choice to analyze the size and the size distribution of the nanoparticle solution [37]. The Brownian motion of the particles dispersed in a liquid can cause fluctuations of the scattered light intensity [37]. This fluctuation of intensity is analysed by the autocorrelated function which calculates the diffusion coefficient of the dispersed particles, and the application of Stokes-Einstein equation determines the hydrodynamic size of the particles scattered in the solution [37]. Adding to that, DLS can present average size of the particles and the size distribution of the particles [37]. Besides low cost and ease of operation, raw data of the measurements from the outcomes of the application is provided by the modern DLS tools that do not require any further mathematical processing [37]. The size distribution of the three different types of capped gold nanoparticles is shown in Figure 3.1. The sizes of the citrate-capped, PVP-capped and TG-capped gold nanoparticles were 40 nm, 33.7 nm and 43.8 nm respectively are calculated as the weighted average values from the DLS measurements shown in Figure 3.1 applying the equation (1).

$$D = \frac{\sum_i^N (I_i d_i)}{\sum_i^N I_i} \quad (1)$$

Here, $\sum_i^N I_i$ = 100 and I_i = scattered light intensity from the particle with diameter d_i.

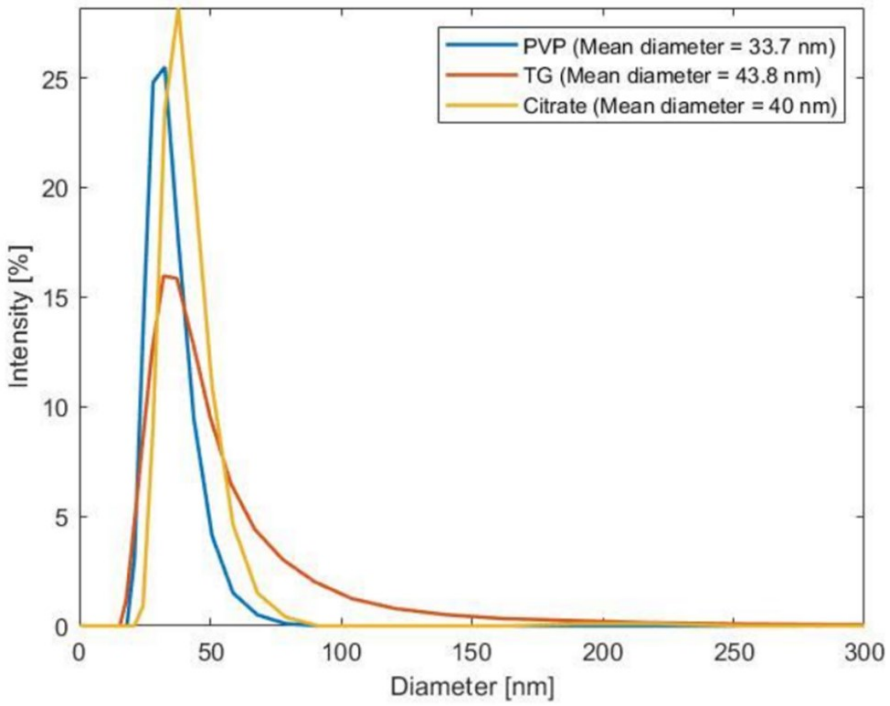

Figure 3.1: Size distribution of three types of capped gold nanoparticles from the obtained DLS measurements.

Characterization of nanoparticles with UV-Vis spectroscopy is another common approach to estimate gold nanoparticles size, concentration and aggregation level [38]. UV-vis spectrometers are easily available in the lab facilities and any alteration of the sample is not required for the analysis. As a result, the registration of the spectrum consumes minimal time. The absorption spectrum generated from the UV-Vis spectroscopy can provide information on the surrounding dielectric medium environment of the nanoparticles [38]. In UV-Vis spectroscopy, spectrophotometers apply light source in the range of UV to the visible wavelength range on the sample to measure the light absorbed, reflected or transmitted from the sample at each

illuminating wavelength. The results of UV-vis spectroscopy in Figure 3.2 are obtained from BioTek Synergy HT UV-Vis spectrometer. Results show citrate-capped gold nanoparticles underwent the highest absorption among the three types of gold nanoparticles, something that is possible because citrate-capped gold nanoparticles need the fewest cleaning cycles. Capping with larger molecules often causes red shift of the resonance peaks, as is evident from the UV-vis spectrum of the gold nanoparticles seen in Figures 3.2. Slight red shift with broad spectrum was observed for PVP capped gold nanoparticles when compared with the spectrum of citrate capped gold nanoparticles. This suggests that PVP being a larger molecule compared to citrate and thioglucose, it provides a different dielectric medium. The red shift of LSPR band is depended on the surrounding dielectric medium [39]. That is why red shift of LSPR band for PVP is observed from 530nm to 535nm.

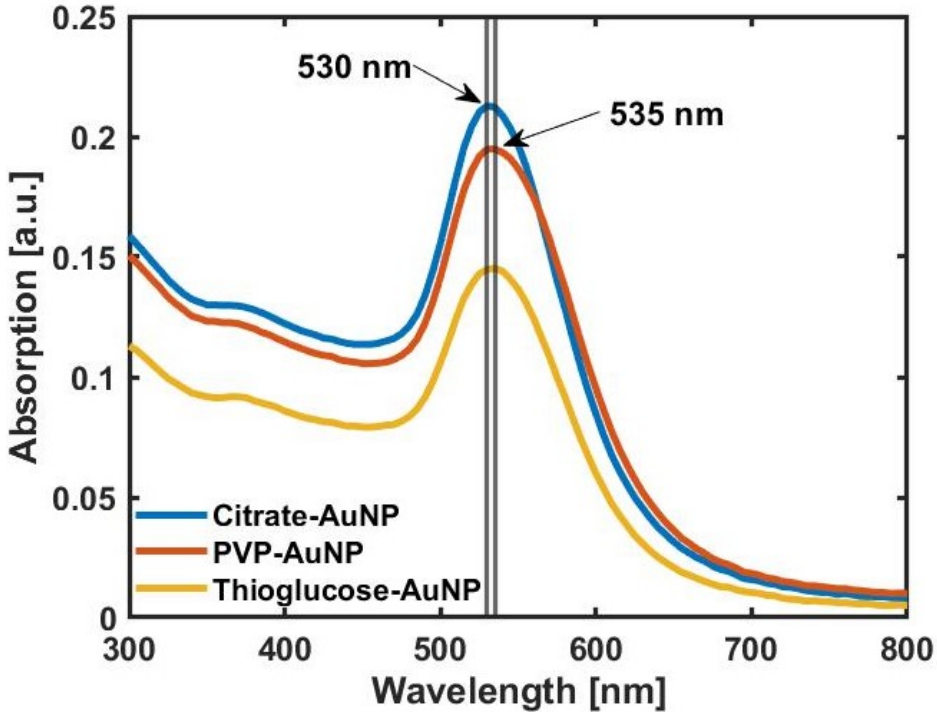

Figure 3.2: UV-vis spectra of three types of gold nanoparticles capped with three different capping agents: citrate, PVP, and TG.

3.5 Experimental setup

Spectral acquisition from single cells was guided by an integrated dark-field microscope system as shown in Figure 3.3 which is conceptualized by the previous PhD candidate of our group and developed by both of us in the lab. The sample developed on the glass slide was attached to a Thorlab xy-direction movable stage. The side of the glass slide with the bacteria was faced towards the laser direction, and a green LED light was used as a source of light to create the dark field. This dark-field setup sent images through a CMOS (complementary metal oxide semiconductor) image sensor camera connected to the low-cost, credit card sized minicomputer- Raspberry Pi. This minicomputer can be plugged into any TV or computer monitor and used for computing in any programming language. In this setup, the Raspberry Pi is connected for a clear view of the bright bacteria cells with nanoparticles or their clusters in a dark background (shown in Figure 3.3), as the high-scattering cross-section of gold nanoparticles added contrast in the image [40]. By adjusting the slide stage, it was possible to bring each sample under the focus of the Coherent LM-785-PLR-100-1K laser used in the system to get the SERS spectra and the laser power was set to 9.78 mW. This laser light was collimated and reflected from an 808 nm notch filter and allowed to shine on the sample through a 0.65 objective lens of the dark-field setup. The Raman signal scattered from the sample then travelled back to the path, where the notch filter rejected the laser wavelength and allowed the Raman signal to be incident on the 0.2 objective lens. Finally, the Raman signal fell on the Kaiser f/18i Spectrograph with a TE-cooled Andor CCD camera controlled by Andor SOLIS software. The integration time used for each run was 60 seconds, with 10 accumulation cycles. Initially, the whole system was calibrated, and distances were adjusted with a test run on dried R6G samples. The condenser lens used in the setup to create the dark field was a water immersion lens

whose numerical aperture (NA) was 0.85, and thus a droplet of deionized water on the glass slide facing the lens was necessary to get the dark-field output.

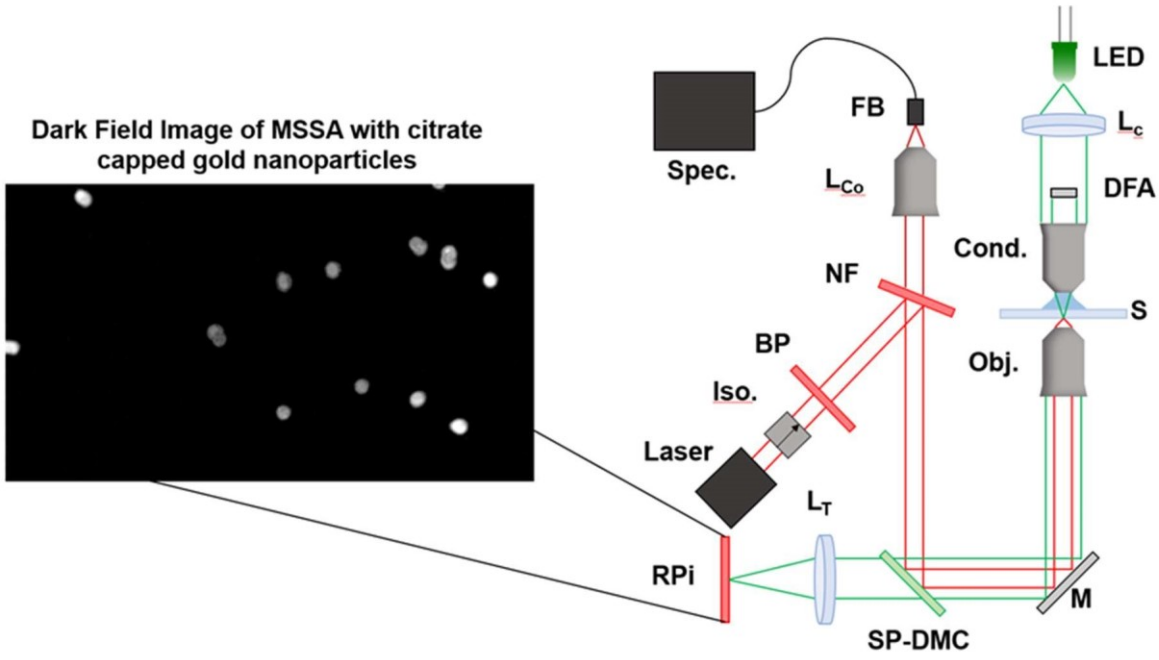

Figure 3.3: Schematic of Raman spectrometer/dark-field microscope used in this work. The components in the diagram are the laser, isolator (Iso.), 785 nm bandpass filter (BP), 808 nm notch filter (NF), short pass dichroic mirror (SP-DCM), the microscope mirror (M), the 0.65 NA objective lens (Obj.), the sample (S), the 0.85 NA condenser lens (Cond.), the dark-field aperture (DFA), the collector lens (L_c), the green LED, the tube lens (L_T), the fiber coupling lens (L_{Co}), the multimode fiber bundle (FB), and the spectrometer (Spec.).

3.6 Sample preparation for bacteria slides

Three of the species of bacteria used in the experiment, Staphylococcus aureus (ATCC 25923, methicillin-sensitive S. aureus, or MSSA), E. coli (CFT073) and C. acnes (ATCC 6919), were acquired from ATCC. The methicillin-resistant Staphylococcus aureus (MRSA) strain (S. aureus BP017), a clinical isolate, was obtained from The Ottawa Hospital. Ethical approval was obtained from the Ottawa

Health Science Network Research Ethics Board to use the C. acnes bacterial strains collected from periprosthetic joint infection patients for this study. Each of the four bacteria samples was mixed with the nanoparticle solution in a microfuge tube in the ratio of 1:9 and given a slight shake. Some drops of the mixture were spread onto a glass slide and then allowed to settle there for 1 hour. After 1 hour, the bacteria were heat-fixed to the slide and the liquid was aspirated, then the slide was dried under a stream of clean filtered air. Finally, the slide was rinsed in a gentle stream of deionized water to remove un-fixed cells and loosely bound debris, then dried again with air. This process was repeated 3 times to ensure enough bacteria had adhered to the slide for measurement.

3.7 Data analysis

All Raman spectra were processed using MATLAB. In this approach, the background subtraction was performed using the adaptive iteratively reweighted Penalized Least Squares (airPLS) algorithm [41]. The spectra were divided by the highest observed intensity in order to normalize and conduct the classification analysis. Spectra from bacteria samples also contained the spectrum of the background matrix, which was also subtracted as background noise.

After background filtration, the data sets were classified and analyzed using genetic algorithm support vector machine (GA-SVM). The GA-SVM method was applied following the analysis and algorithm developed by Hunter et. al. [42]. In this GA-SVM approach, hyperparameter selection for complex kernel functions was accomplished by using a classical genetic algorithm. A kernel function κ is a metric of similarities between two points. So, SVM uses this kernel function to compare between data points and use its feature space to construct an optimal hyperplane that

works as a separation line in the data sets. The rational quadratic kernel (RQK) is used here for classification, which is an infinite sum of exponentiated quadratic Kernels as understood from equation (2)

$$\kappa_{RQK} = \sigma^2 \left(1 + \frac{(\chi_i \chi_j)^2}{2\alpha l^2}\right)^{-\alpha} \quad (2)$$

Here, χ is the data set obtained from the processed Raman spectra, with χ_i and χ_j representing samples from it [43], and σ, α and l are the hyperparameters of the kernel that are selected by the genetic algorithm. Since in this case multi-class classification was required for data analysis and results interpretation, "one-against-one" multi-binary classifier method was applied on the data sets. Data sets were divided in two groups: a training set (60%) and a test set (40%). The training set was used to develop the discriminant analysis model, and the test sets were used to validate the model. To obtain the SERS spectra, 10 spectra were averaged to get an averaged spectrum for each bacteria cell, 3 respective background spectra were averaged and then subtracted from the averaged spectrum of the individual bacteria. At the end, baseline correction was applied using airPLS.

PLS-DA was then applied on the data sets to understand which Raman bands, and the number of unique peaks, contributed to our discriminant analysis. PLS-DA which stands for Partial Least Square Discriminant Analysis is a classification method that is utilized for predictive and descriptive modelling along with selection of discriminating variable selection. In this approach of classification, dimensionality reduction is combined with discriminant analysis for high dimensional data modelling [44]. This reduction is needed because spectral data have large number of variables and dimensions. In this situation, ordinary least square solution fails or cause overfitting of the model. To avoid these issues, multivariant tools are required to continue modelling and discrimination [9]. Thus, PLS-DA is a

common technique applied on Raman data for discriminant analysis. Table 1 shows the PLS-DA outcomes for TG capped gold nanoparticles in bacteria species identification and strains discrimination of *S. aureus*. PLS-DA achieved an overall discriminant accuracy of 80% when trained on 60% of the data and validated on the remaining 40%. Furthermore, the scatter plot in Figure 3.4 for TG illustrates that the bacteria form distinct clusters in the first two scores whose associated loadings describe 55% of the total covariance. These results illustrate the validity of performing Raman band assignment using the first two loading vectors. Figure 3.5, show the first and second loading vectors of the thioglucose capped gold nanoparticles with positive and negative peaks in each loading. The baseline correction by airPLS algorithm was done for each plot of the loading vectors of three different capped gold nanoparticles and the Raman bands were assigned. Figure 3.6 shows the plot of first and second loadings for the TG after base line correction. The band assignment showed that discriminating Raman peaks are present in both loadings however, those discriminating Raman peaks are distinct in the second loading. In Figure 3.11, second loading vectors for all three capping agents are shown for Raman band assignment.

Table 1: PLS-DA of TG capped gold nanoparticles in bacteria detection

	E. coli	MRSA	MSSA	*C.acne*
Thioglucose	100%	55%	50%	98%

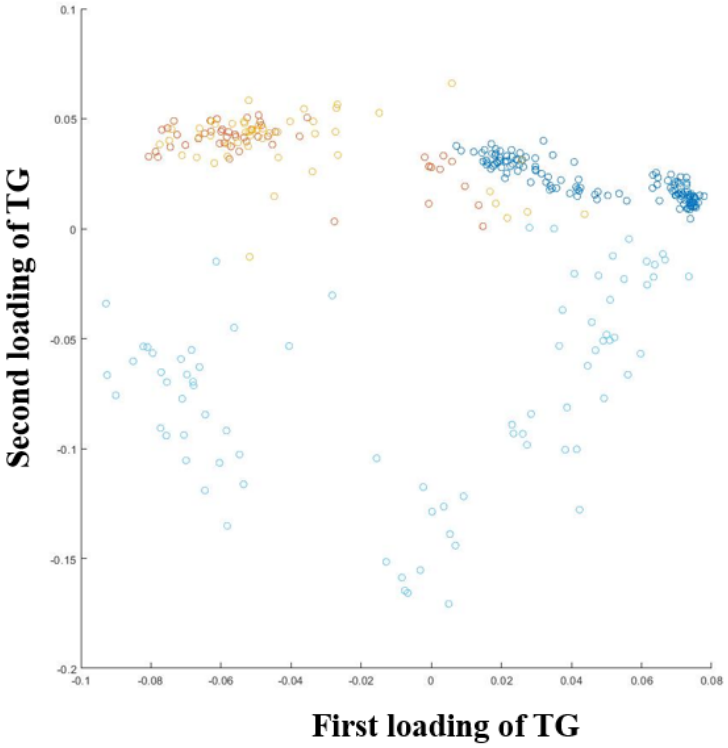

Figure 3.4: Scatter plot of loadings for TG

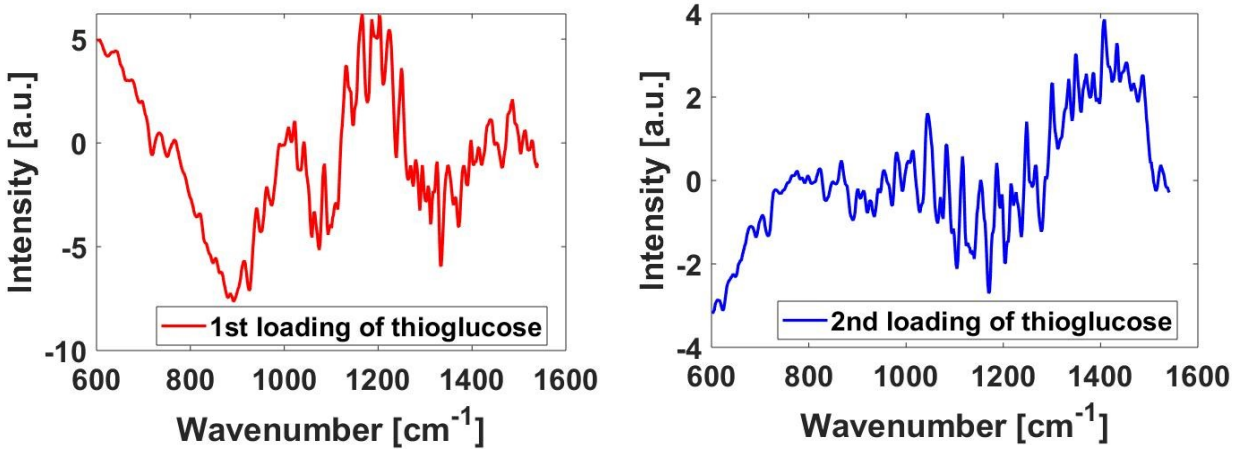

Figure 3.5: First and second loading vectors for the TG.

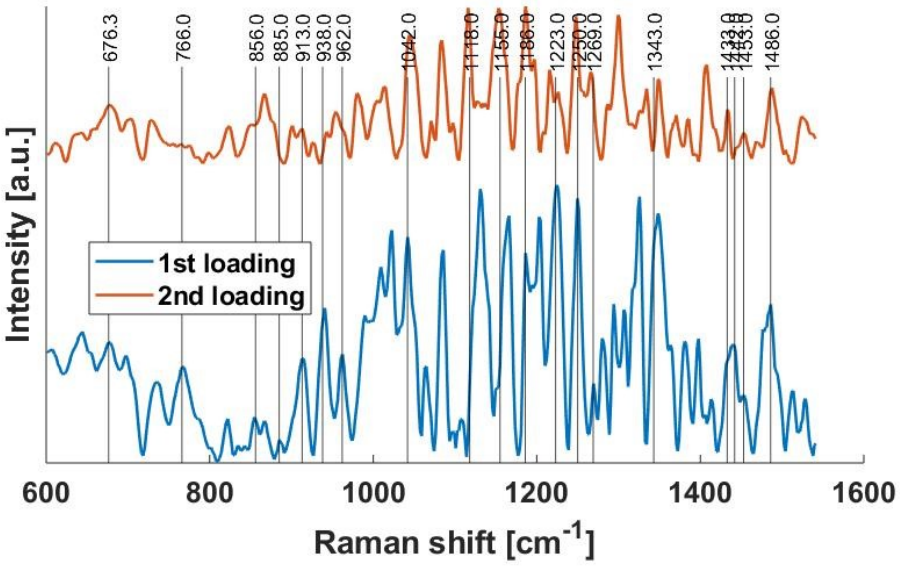

Figure 3.6: First and second loadings of TG after baseline correction

3.8 Results of optimization of capping agents

The three types of capped gold nanoparticles were dried on glass slides, and the Raman spectra from each were collected to confirm the successful coating of TG and PVP capping agents by the replacement of citrate. As seen in Figure 3.7, several Raman bands in TG and PVP spectra demonstrate that the bindings were successful in the gold nanoparticles. The peak at 505 cm^{-1} and 824 cm^{-1} in TG spectra corresponds to the Au-S bond and CS ring respectively [45]. These peaks are absent in the spectra for citrate capped gold nanoparticles, and the presence of thiol group (S) in the bonds confirms the successful binding of TG with gold nanoparticles displacing the citrate. In the spectrum for PVP-capped gold nanoparticles, the Raman band ranging from 1495 cm^{-1} to 1661 cm^{-1} corresponds to the vibrations produced by C-N and C=O bonds of the lactam ring that came from PVP attached to the gold nanoparticles [46].

Another peak at 652 cm^{-1} corresponds to the N-C=O bend from PVP [46]. These band ranges are also absent in the spectrum for citrate-capped gold nanoparticles, confirming the adsorption of PVP by the gold nanoparticles. However, the overlap of the bands with citrate-capped gold nanoparticles suggests that at some sites of the gold nanoparticles, the citrate displacement could not be completed.

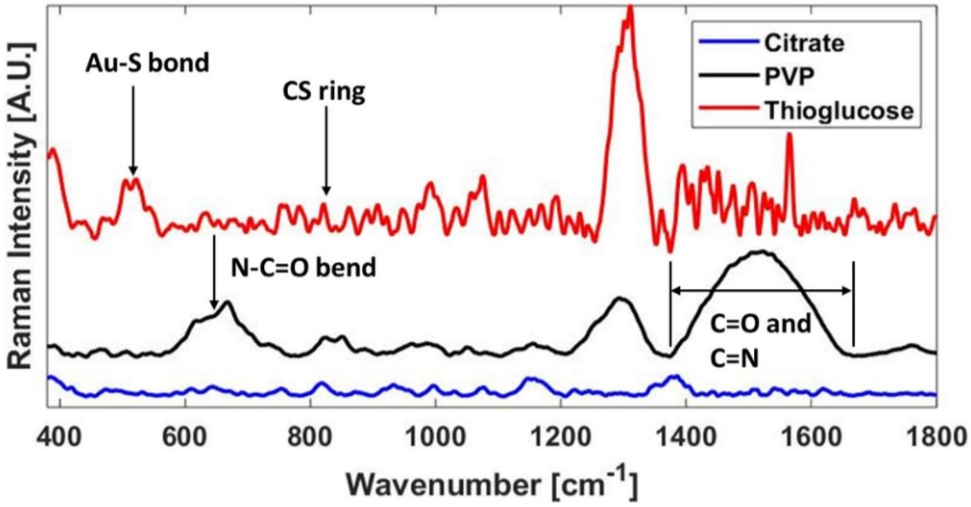

Figure 3.7: Spectra from three types of gold nanoparticles capped with three different capping agents: citrate, PVP, and TG.

The bacterial sample slides with capped gold nanoparticles were mounted in the navigation stage, which, under adjusted focus, showed a clear view of a section of the slide in the CMOS camera, as demonstrated in Figure 3.3. The CMOS camera assisted again in adjusting the laser beam and tightly focusing the beam on the bacterial cell. 35 cells per class were measured taken over three independent cultures of bacteria. Approximately 10 spectra were collected per cell. Figures 3.8 and 3.9 show the mean of 100 spectra for each species. The standard deviation is shown overlaying on the SERS signal obtained for *E. coli* with citrate capped gold nanoparticles in the Figure 3.10 and the calculated signal to noise ratio (SNR) is 9.8 db. The PVP-capped nanoparticles consistently yielded the highest number of distinct Raman peaks, with high intensities in the observed SERS spectra for all three

species of bacteria in the experiment and both strains of S. aureus (as shown in Figures 3.8 and 3.9). In addition, Figure 3.9 shows that Raman spectra were consistent for both citrate-capped and TG-capped gold nanoparticles with all species and strains of bacteria in the experiment.

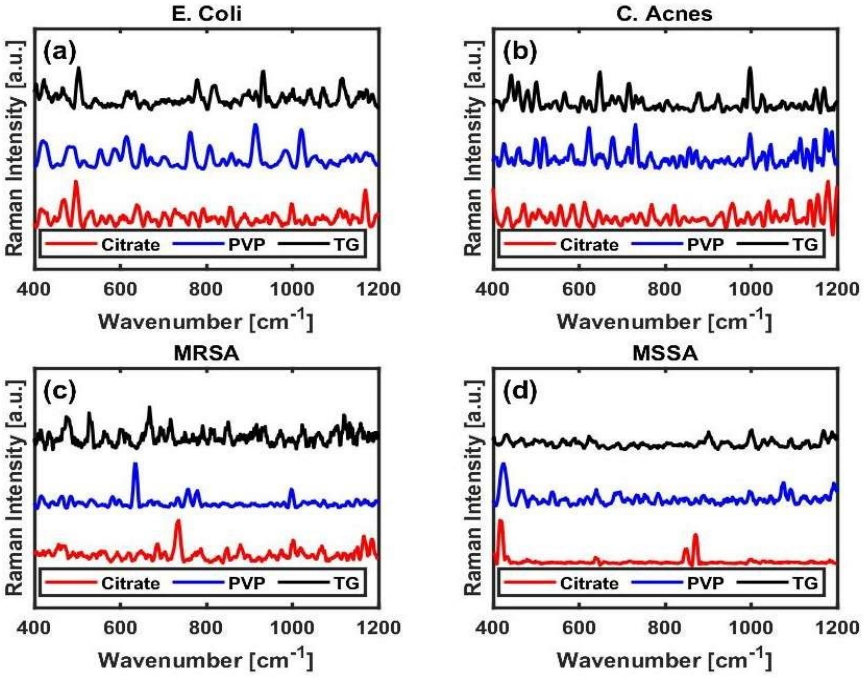

Figure 3.8: SERS spectrum of (a) E. coli (b) C. acnes (c) MRSA and (d) MSSA with three different capped gold nanoparticles.

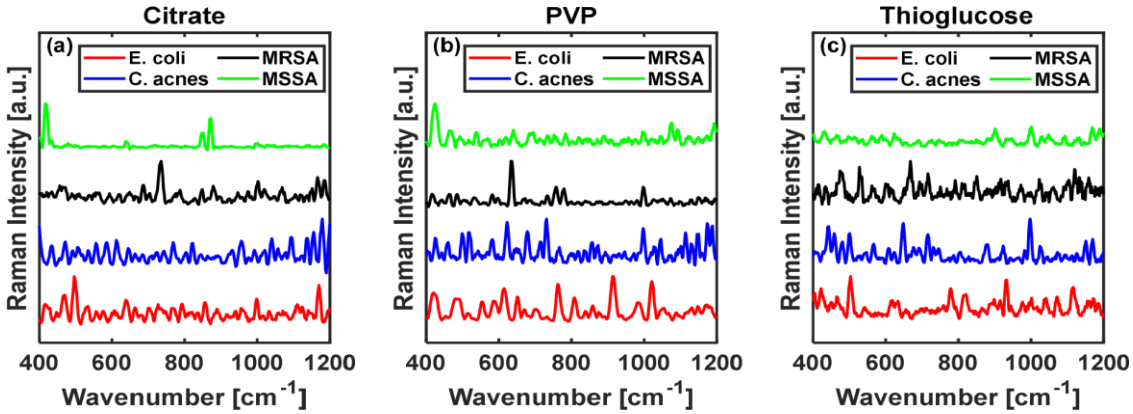

Figure 3.9: SERS spectrum of all species and strains of bacteria with (a) citrate capped gold nanoparticles (b) PVP-capped gold nanoparticles and (c) TG-capped gold nanoparticles.

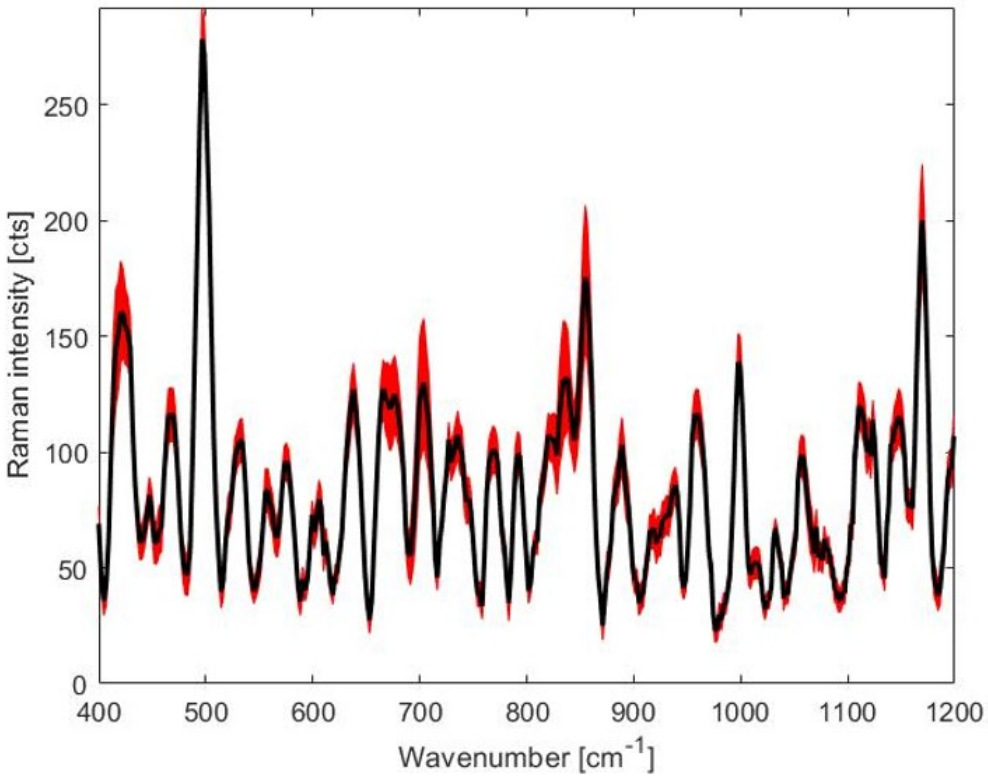

Figure 3.10: Standard deviation overlaid on the SERS spectrum of E. coli with citrate capped gold nanoparticles.

3.9 Performance of capping agents in species and strain identification

350 SERS spectra of each bacteria species were then analyzed using SVM discriminant analysis to compare the effect of capping agents on spectral discrimination. Tables 2 and 3 show the species and strain identification accuracy obtained with different capping agents. The results show that both citrate and TG particles are better discriminants for species than PVP particles are. Moreover, as shown in Table 3, TG is superior among the three in the identification of two strains of S. aureus: MRSA and MSSA, which suggests that any bio-functionality gained by the addition of TG results in a SERS substrate amenable to bacterial detection.

Table 2: Species identification accuracy with different capping agents ($p < 0.01$ in all cases, compared to null hypothesis of prediction of 33.3%)

Species	Citrate	TG	PVP
C. acnes	97.8%	95.6%	63.6%
E. coli	96.2%	100%	85%
S. aureus	100%	89.7%	83.3%

Table 3: Strain identification by different capping agents ($p < 0.01$ in all cases, compared to null hypothesis of prediction of 50%)

Strain	Citrate	TG	PVP
MSSA	85.2%	91.4%	77%
MRSA	80.8%	87.7%	60%

3.10 Discussion

The results in Table 2 and 3 would appear to be counterintuitive based on the previous results in Figures 3.8 and 3.9, which showed that the PVP particles yielded the highest-intensity spectra. It may be the case that PVP-capped gold nanoparticles attached to bacteria cell sites and structures that were conserved across the bacteria, thus resulting in poor spectral discrimination. Better percentage of accuracy can be achieved with citrate than with PVP in both species and strain detection. This can be explained from studies that have found citrate-capped nanoparticles easily stick to the cell wall, as the citrate layer can be replaced effortlessly by the proteins of the bacteria cell wall, and the charge effect of the metallic nanoparticles allows to bind strongly to the cell surface [12, 47]. Among the three capping agents applied, TG (which has not been applied previously in SERS analysis of bacteria) yielded a surprisingly good response in species identification and produced the best response in discriminating MRSA and MSSA.

To explore the outcomes further, we considered the importance of different Raman spectral features by analyzing the loading vectors of PLS discriminant models. The spectra from the second loading vectors of PLS for the three types of gold nanoparticles with bacteria in Figure 3.11 helps to identify the contribution of Raman bands by assigning the bands to different cell elements [12, 48, 49, 50].

Since the gold nanoparticles were capped with three different capping agents, the spectral features seen in Figure 3.11 include Raman bands from metabolic secretions of the cell and the cell wall components [12]. Capped gold nanoparticles can penetrate inside the cell and adsorb to the cytoplasmic membrane and organelles [12]. The individual spectral features of citrate-capped and TG-capped gold nanoparticles with bacteria cells in Figure 3.11 shows multiple ranges of strong peaks in Raman bands for four nucleic acid components (adenine, guanine, cytosine, uracil and thymine) [12, 48, 49, 50]. Nucleic acid components are the basic components that create genetic differences in strains of a species. However, PVP showed weaker peaks for only two of the nucleic acid components (adenine and guanine: 1326 cm^{-1} to 1343 cm^{-1}) [12, 48, 49, 50]. PVP produced distinctive peaks in the Raman spectrum for the general cell body components existing in a typical bacteria cell. As a result, although PVP was efficient in producing high-intensity Raman peaks in the observed SERS spectrum, it provided a weak response in discriminating the species and strains of bacteria.

The spectra from TG-capped gold nanoparticles with bacteria in Figure 3.11 shows the highest number of Raman bands for the nucleic acid components among the three types of capped gold nanoparticles. The Raman bands with TG-capped gold nanoparticles can be assigned at 1265 cm^{-1} (cytosine); 665 cm^{-1} (guanine), 640 cm^{-1} (tyrosine), 729 cm^{-1} to 824 cm^{-1} (cytosine, uracil, tyrosine, adenine and thymine); 1300 cm^{-1} to 1400 cm^{-1} (adenine, guanine, and cytosine) [12, 48, 49,

50]. This suggests that TG-capped gold nanoparticles, by binding strongly with nucleic acid components, collect more information about genetic difference among the species and strains than the other two capping agents collect. For this reason, TG stands out as the best for both species and strain identification.

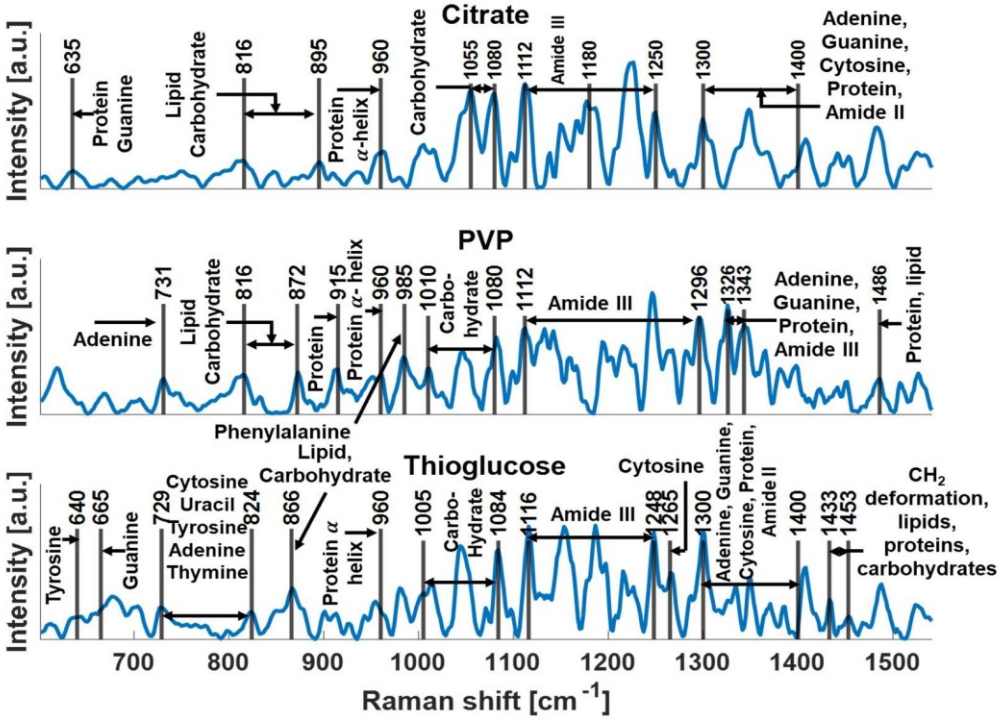

Figure 3.11: Spectra of the PLS loading vectors for the three capping agents: citrate, PVP, and TG.

Despite these differences, all three spectra for the three capping agents have Raman peaks for some common components among them, e.g., lipid – carbohydrate (816 cm^{-1} to 895 cm^{-1}), protein α- helix (960 cm^{-1}), Amide III (112 cm^{-1} to 1250 cm^{-1}) [12, 48, 49, 50]. This suggests that three of the capping agents can attach well with the bacteria cell to enhance the Raman scattered signal.

3.11 Conclusion

In summary, the capping agent is a vital factor in controlling the pattern and functionality of metallic nanostructures in SERS. As a result, it can play a significant

role in interactions with target molecules and achieve distinctive features from the enhanced Raman signals. In this study, we selected three capping agents, thioglucose, polyvinylpyrrolidone (PVP) and citrate, which were applied in SERS detection of species and strains of bacteria. The collected SERS data under the genetic support vector machine algorithm and discriminant analysis showed that PVP provided minimal response in species or strain discrimination, although it had the strongest Raman intensity peaks among the three capping agents. However, thioglucose proved to have good efficiency in species detection of bacteria and showed the highest accuracy in strain discrimination among the three applied capping agents. Citrate, which is commonly applied in SERS of bacteria, lagged behind thioglucose in strain identification. This demonstrates that thioglucose has the potential to be an excellent capping agent in SERS detection of pathogens, particularly in detecting MRSA and MSSA. Moreover, understanding the mechanism of its interaction as a surfactant in SERS detection requires further investigations in the field of SERS on micro living cells.

Chapter 4 Study of SERS application on shoulder tissue

4.1 Introduction

Periprosthetic joint infections are painful for patients yet difficult to diagnose. The infections are usually caused by pathogens that are hard to detect. The purpose of the research described in this chapter is to explore if SERS can be used to detect shoulder tissue infections and to develop a valid diagnostic test for such infection. A literature review revealed that SERS was never used in the diagnosis of shoulder tissue infections. Consequently, a detailed SERS study was designed to find the optimal conditions needed to maximize the Raman signal. For this study, ex-situ SERS, in-situ SERS methods and the combination of both methods were applied on the shoulder tissue samples. Tissue samples were incubated in the citrate capped gold nanoparticle solution in the ex-situ SERS method. Citrate capped gold nanoparticles were selected for this project as it is more often used in the biomedical applications. For the in-situ SERS method, UV exposed photochemical reaction was utilized to generate gold nanoparticles in the tissue samples from the gold precursor solution. In the approach of ex-situ and in-situ applied together, the samples were incubated first in citrate capped-gold nanoparticle solution and then exposed to UV light with gold precursor solution.

4.2 Periprosthetic joint infection and application of SERS

Shoulder joint replacement surgery, or shoulder arthroplasty, can have serious risks and complications. One is periprosthetic joint infection (PJI), a rare but serious complication. This infection is now one of the frequent reasons for painful shoulder arthroplasties [51]. Skin pathogens such as *Cutibacterium acnes* (*C. acnes*) and Staphylococcus sp. are usually responsible for this infection [51]. Although 31% to

70% of prosthetic shoulder joint infections are associated with C. acnes, this microorganism is hard to detect because of its slow growth [51, 52, 53, 54]. In addition, infection from the antibiotic-resistant Staphylococcus strain cannot be treated with broad range antibiotics until detected, and this strain is hard to identify until it forms biofilm around the new implant [51]. PJI can show up as an acute early infection or a chronic late infection. Due to the large variance in the types of infecting pathogens, it is beneficial to confirm the identity and antibiotic-resistant strain of the infecting pathogen at the preoperative diagnosis stage. This confirmation and information about the infecting pathogen at the surgical site can help to modulate the cement used in arthroplasty with proper antibiotics for the pathogen of concern.

Two types of methods are applied to diagnose the infecting pathogens: direct and indirect [51]. Direct methods both confirm the infection and detect the pathogen, while indirect methods confirm only the infection. Direct methods, such as aspiration or biopsy of synovial tissue, are therefore preferred [51]. Aspiration allows for specific and nonspecific tests, such as cell count determination, the leucocyte esterase strip test, and the alpha-defensin synovial fluid biomarker assay [51]. Synovial tissue can also be analyzed using PCR methods; however, PCR has great potential to produce false positive results that can mislead the treatment. Biopsy allows for a combination of tests, thereby improving the potential accuracy of the diagnosis to achieve 100% specificity and sensitivity [51].

Surface-enhanced Raman spectroscopy (SERS) is an evolving technique in detecting biomolecules and pathogens that could be applied to synovial tissue samples collected by biopsy preoperatively and intra-operatively. A data comparison of the preoperative and intra-operative tissue samples could help to determine a valid diagnosis for the PJI. Using SERS to diagnose an infection could eliminate the need to revalidate a diagnosis by running multiple experiments using different antibodies.

4.3 Experimental setup

The setup for this optimization experiment was the same SERS setup detailed in Section 3.3 of Chapter 3 of this thesis. However, for this experiment the darkfield aperture (DFA) was removed to generate bright field image of the tissue samples (as shown in Figure 4.1). Bright field image allowed clear vision of the tissue samples. The glass slides with the samples prepared under various conditions (as detailed below) were placed in the navigation stage to collect data from the Raman signal that fell on the Kaiser f/18i Spectrograph. The integration time used for each run was 60 seconds with 10 accumulation cycles. Later for image scanning, GVSM002-US/M - 2D Galvo System and SL50-CLS2 scan lens from Thorlabs were added to the dark-field SERS setup. The spectrometer was also replaced by iHR320 Horiba spectrograph controlled by LabSpec6 software. Figure 4.1 shows the modified experimental setup for scanning microscope in SERS.

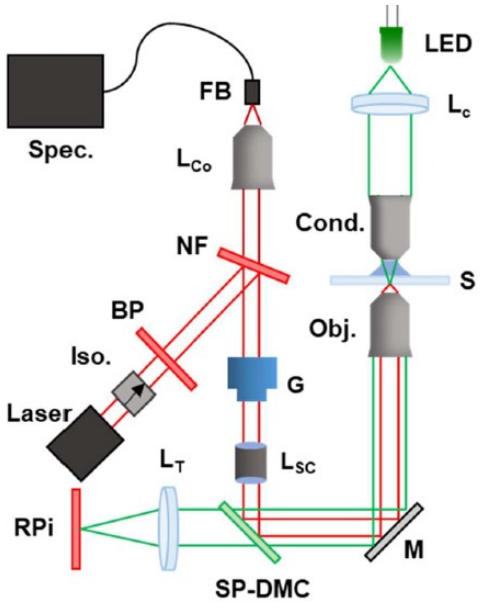

Figure 4.1: Schematic of Raman spectrometer/dark-field scanning microscope used in this work. The components in the diagram are the laser, isolator (Iso.), 785 nm bandpass filter (BP), 808 nm notch filter (NF), galvo system (G), scan lens (L_{sc}),

short pass dichroic mirror (SP-DCM), the microscope mirror (M), the 0.65 NA objective lens (Obj.), the sample (S), the 0.85 NA condenser lens (Cond.), the collector lens (L_c), the green LED, the tube lens (L_T), the fiber coupling lens (L_{Co}), the multimode fiber bundle (FB), and the spectrometer (Spec.).

4.4 UV treatment conditions

In this experiment, SERS spectra were acquired from synovial biopsy samples enhanced with in-situ and/or ex-situ formed gold nanoparticles. In-situ generated nanoparticles are formed by spontaneous oxidation and forced radicalization [55]. It was expected that in-situ formed gold nanoparticles would provide a high-quality spectral fingerprint to diagnose the PJI infection because in-situ generated nanoparticles are expected to remain integrated deep inside the sample itself instead of remaining attached to only outer membrane of the tissue cells. According to the literature, the amount of time required for in-situ gold nanoparticle synthesis varies from 3 seconds to 40 minutes [56, 57, 58].

A two-factorial experimental design with four levels of UV light power and one category of UV exposure time was planned for the optimization purpose. The UV exposure time was 24 hours, and the UV light powers were 5 mW, 10 mW, 20 mW, and 30 mW, for a total of 4 conditions. Each condition was applied on 5 replicates that used a total of 20 samples of the prepared tissue slides. A previous study found that long exposure times at lower power result in the synthesis of larger gold nanoparticles [59]. To achieve Raman excitation with 785 nm wavelength of laser, 40 nm nanoparticles were required with close nanogaps between adjacent nanoparticles [60]. The samples under these 4 conditions were compared with samples incubated with tetrachloroauric acid in the dark for 24 hours to clarify the effect of UV exposure, untreated samples, and samples incubated with pre-

synthesized gold nanoparticles for 24 hours. All conditions were compared based on the SERS amplification obtained for each condition. Samples from the best performing in-situ condition were then combined with pre-synthesized gold nanoparticle incubation to observe if there was any elevated effect in the SERS. All these optimization experiments were performed on the primarily infection-negative slides, since this group contained more slides than the infection-positive group.

4.5 Sample preparation for tissue slides

This experimental work applied on tissue samples was conducted under the project-Diagnostic Accuracy of Synovial Biopsy for Implant-Related Shoulder Infections, for which the ethical approval was obtained from the Ottawa Health Science Network Research Ethics Board. Shoulder tissue samples attached on glass slides were provided by Peter Lapner's research group.

Slides were randomly sorted out first, by placing 5 slides in one set to apply different conditions of nanoparticles generation or fabrication. These multiple methods of nanoparticle integration with tissue samples were carried out to compare their SERS outcome.

After the sets of slides were sorted, each set was heated up in a bio-friendly oven at its labelled low scale for 20 minutes so that the paraffin coating bonds get loose to take off easily in the deparaffinization process. During this time, a soap solution was prepared by mixing 0.8 g of dish cleaning soap with 400 ml of water. This solution was needed to clean the paraffin film coat on the tissue samples used to stick them to the glass slides initially. The soap solution was then heated up to boil on a hot plate in a beaker at 170℃. On another hot plate, two heavy, glass slide- staining dishes were placed side by side, covered with aluminium foil (to confine the heat inside to expedite the heating process) and heated at 90℃. Once the soap solution

started to boil, 200 ml were poured immediately into each slide- staining dishes on the hot plate.

By this time, the slides had completed heating up and were taken out of the oven. With the help a of a slide rack, they were all immersed in one of the dishes filled with soap solution and kept immersed for 2 minutes. After 2 minutes, they were transferred to the next dish and immersed again in clean soap solution for another 2 minutes. Then each slide was cleaned for 5 minutes in hot tap water and deionized water.

An anti-buffer solution had been prepared earlier by mixing 2.184 g of sodium citrate and 0.302 g of citric acid to a bottle of 900 ml of deionized water. Then, 0.45 ml of Triton were added to the solution and mixed well for 15 to 20 minutes via inversion. The beaker 200 ml of anti-buffer solution was then heated up on a hot plate to boil.

A new slide staining dish was covered with foil and placed on another hot plate at 90℃ to heat up. As soon as the solution started boiling, it turned foggy, and it was poured immediately in the dish on the hot plate. The cleaned slides were then immersed in this hot anti-buffer solution for 30 minutes. Each of the slides was then cleaned for 5 minutes in deionized water and dried for 10 minutes in the oven. The dried slides were then placed in the UV-reactor slots developed in the lab by a PhD student in our group.

Citrate-capped gold nanoparticles were synthesized following the recipe described in Subsection 3.2 of Chapter 3 of this thesis. According to the ex-situ and in-situ conditions of gold nanoparticle integration into tissues, they were kept inside the reactor with the required power and time frame designed for the conditions. The nanoparticles attached to the tissue turned some spots of the samples into black (as shown in Figure. 4.2), which suggests that these spots have junctions that

nanoparticles will attach to or that these spots produce the desired gold nanoparticles as per the treatment applied on them.

Figure 4.2: Slides in UV reactor slots after gold nanoparticle integration to the tissue samples.

4.6 Data analysis

All Raman spectra were processed using MATLAB. In this approach, the background subtraction was performed using the adaptive iteratively reweighted Penalized Least Squares (airPLS) algorithm [41]. For each tissue sample, 10 SERS spectra were collected along with 3 background spectra. Average of background spectra was subtracted from the averaged SERS spectra prior to application of airPLS on SERS spectra. The spectra were divided by the highest observed intensity in order to normalize. The Raman integral is calculated from the normalized spectra to compare each condition applied to the samples.

4.7 Results and analysis

4.7.1 SERS optimization

To apply SERS experiment on shoulder tissue and to optimize the method for the purpose of infection diagnosis, eight combinations of conditions were applied to create eight different sample sets. They are summarized in the following table.

Table 4: Summary of conditions of the experiment process.

	Type of nanoparticle integration	UV power (mW)	UV reactor time (hrs)	Citrate particles	Gold solution
Set A	Raw sample	0	0	Not added	Not added
Set B	In-situ	0	24	Not added	Added
Set C	Ex-situ	0	24	Added	Not added
Set D	In-situ	5	24	Not added	Added
Set E	In-situ	10	24	Not added	Added
Set F	In-situ	20	24	Not added	Added
Set G	In-situ	30	24	Not added	Added
Set H	In-situ + ex-situ	20	24	Added	Added

Sets B, D, E, F, and G allowed in-situ gold nanoparticle integration to the tissue samples, and Set C allowed ex-situ gold nanoparticle integration. Set H was treated with both ex-situ and in-situ nanoparticles; the 5 samples in Set H were incubated

for 24 hours in citrate capped gold nanoparticle solution, and then 20 mW of UV power was applied to the samples incubated in gold solution for 24 hours.

The ex-situ method of sample preparation provided externally attached citrate capped gold nanoparticles to the samples, while the in-situ method generated gold nanoparticles inside the tissues on the slides. Colloidal synthesis and the application of nanoparticles on the samples required delicate control of the nanoparticles' morphological features to maximize the SERS effect. Advancement in nanotechnology has shown how the photoreduction process can contribute to the formation of crystal-based gold nanoparticles [61]. The UV radiation of different wavelengths can induce photochemical reactions in gold solutions, and the available biomolecules in the cell membranes in the presence of surfactants can control the dimensions of the generated gold nanoparticles [61].

The 100 spectra were collected from ten different spots on each tissue slides and 3 spectra were collected from blank spot to capture the background spectra. The average of 3 background spectra were subtracted from the average of 100 tissue spectra as shown in Figure 4.3.

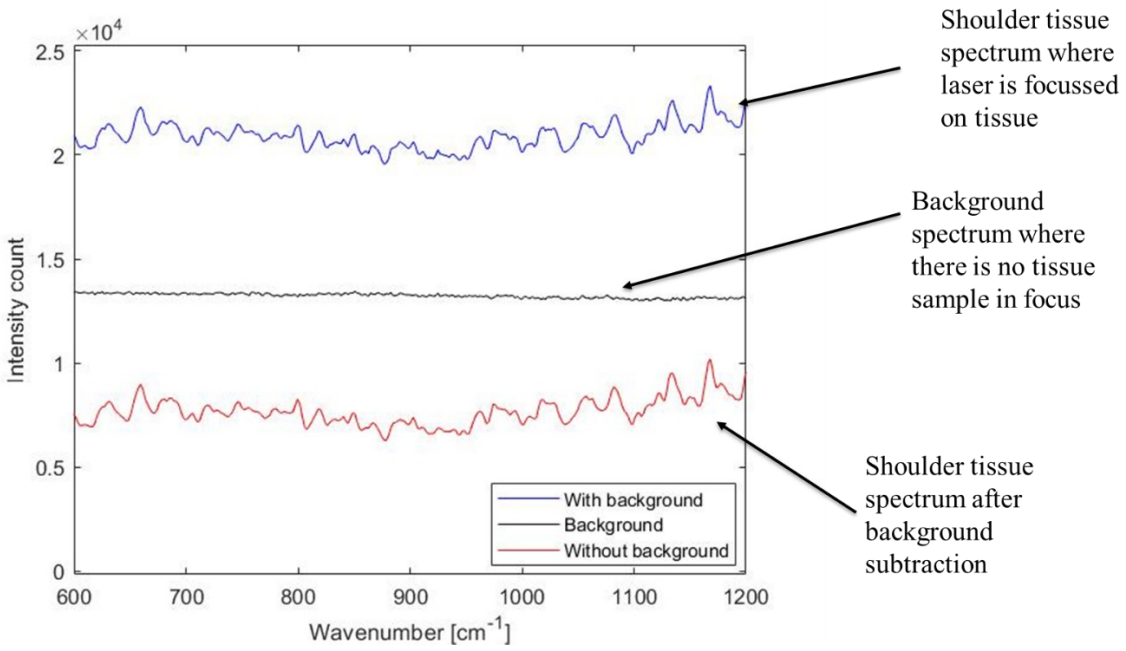

Figure 4.3: Shoulder tissue spectrum after background subtraction.

Figure 4.4 shows the comparison of SERS spectrum for the first three sets: A, B, and C. These results confirm our expectation that the raw samples cannot provide a strong SERS signal. Figure 4.4 also suggests that the dark-field environment cannot create any in-situ gold nanoparticles in the cells of the tissue, and therefore the intensity counts for that set (Set B) are very low. However, the surge in intensity counts can be noticed in Set C, where citrate-capped gold nanoparticles were incorporated ex-situ through 24 hours of incubation. This suggests that a sufficient amount of citrate-capped gold nanoparticles can attach to the shoulder tissue to provide a strong SERS signal.

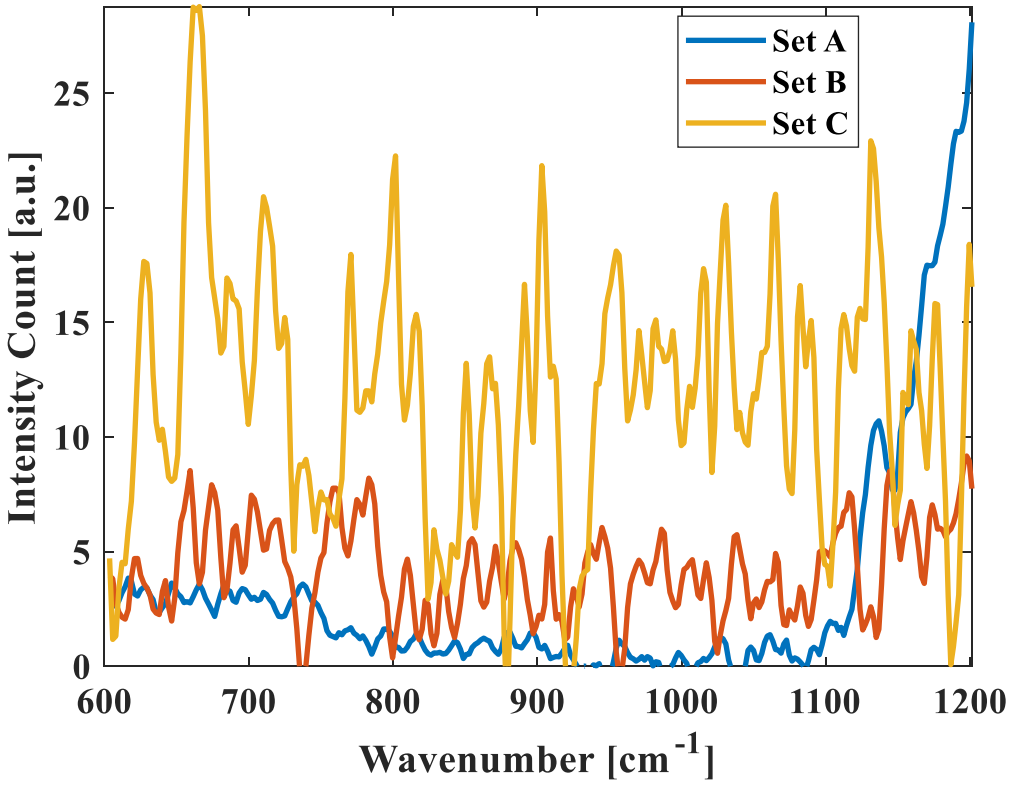

Figure 4.4: Comparison of SERS spectra from Sets A, B, and C.

The UV reactor developed in our group is controlled by a microcontroller based on an Arduino system. It can provide power input from 1 mW to 30 mW. Therefore, to confirm in-situ generation of gold nanoparticles in tissue and understand which power strength would work the best in inducing a strong photochemical reaction for in-situ gold nanoparticle formation in the shoulder tissue samples, the UV reactor was run initially at 5 mW, and then the power was increased for the next sets of samples. Figure 4.5 shows that 5 mW (Set D) is not enough to produce sufficient gold nanoparticles to render strong SERS from tissue samples.

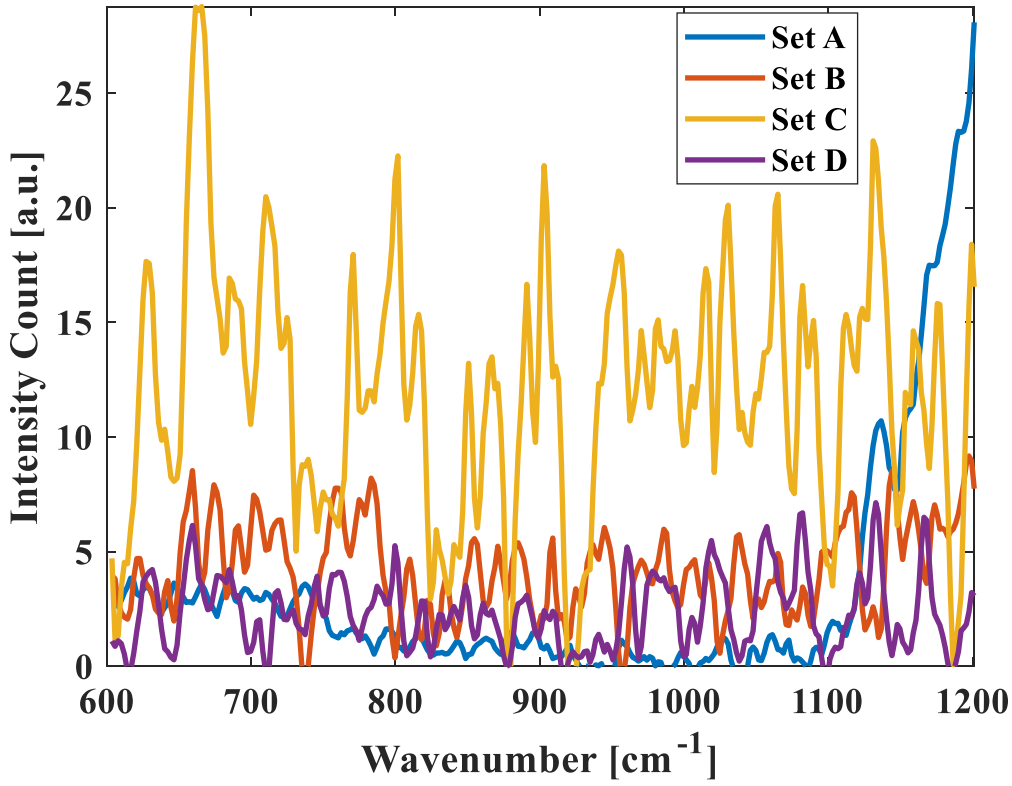

Figure 4.5: Comparison of SERS spectra from Sets A, B, C, and D.

The UV power was then gradually increased to the maximum value of 30 mW, and the corresponding SERS spectra were collected. Comparison of all these spectra suggested that 20 mW is the optimum power of the UV reactor that can generate potentially strong and sufficient in-situ gold nanoparticles in the shoulder samples (as seen in Figure 4.6), as it gives the highest integrated spectral intensity among all applied UV powers.

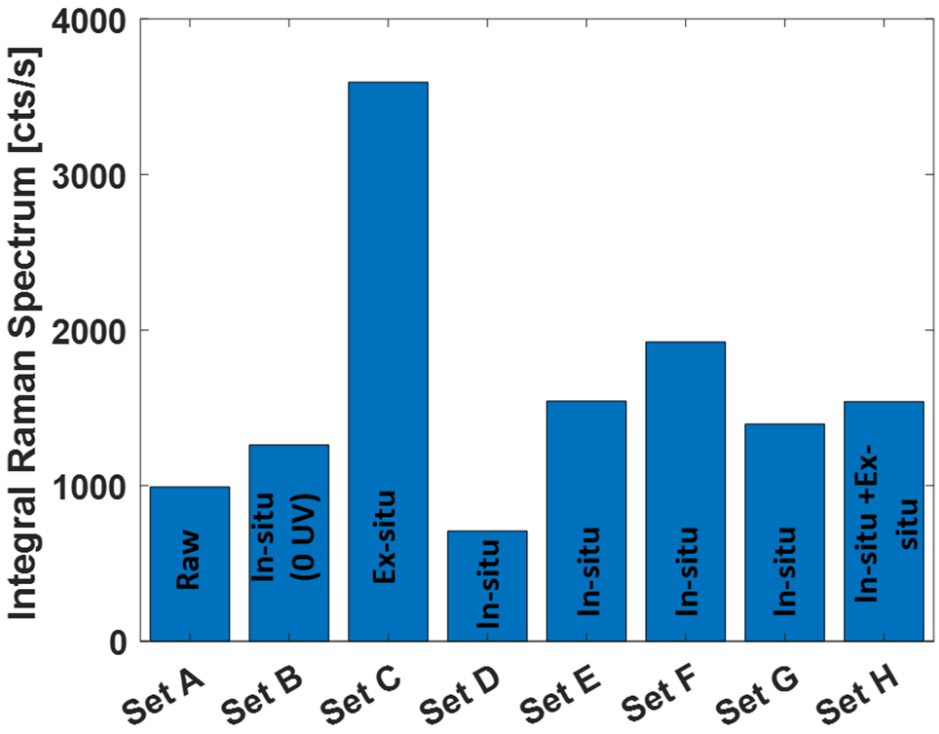

Figure 4.6: Comparison of integral spectral intensity from SERS spectra of Sets A, B, C, D, E, F, G, and H.

Comparing all the sets in Figure 4.5 shows that among all UV power strengths applied in this experiment, 20 mW provided a strong response in producing SERS signal with in-situ gold nanoparticles. Further, the ex-situ integration of gold nanoparticles in Set C provided a better response than the in-situ formation of gold nanoparticles in shoulder tissue samples at 20 mW in Set F.

To confirm this scenario, another new set of samples (Set I in Table 5) were used to test ex-situ integrated gold nanoparticles condition. For Set I, sample slides were incubated for 24 hours in citrate-capped gold nanoparticles. Another set of samples (Set J in Table 5) was also tested combining the ex-situ and in-situ conditions. Then the SERS data were collected in the dark-field microscope setup. The results were compared with the previous outcomes in Figure 4.7.

Table 5: New sets used to confirm the results from the ex-situ method and combination of ex-situ, in-situ methods.

	Type of nanoparticle integration	UV power (mW)	UV reactor time (hrs)	Citrate particles	Gold solution
Set I	Ex-situ	0	24	Added	Not added
Set J	In-situ + ex-situ	20	24	Added	Added

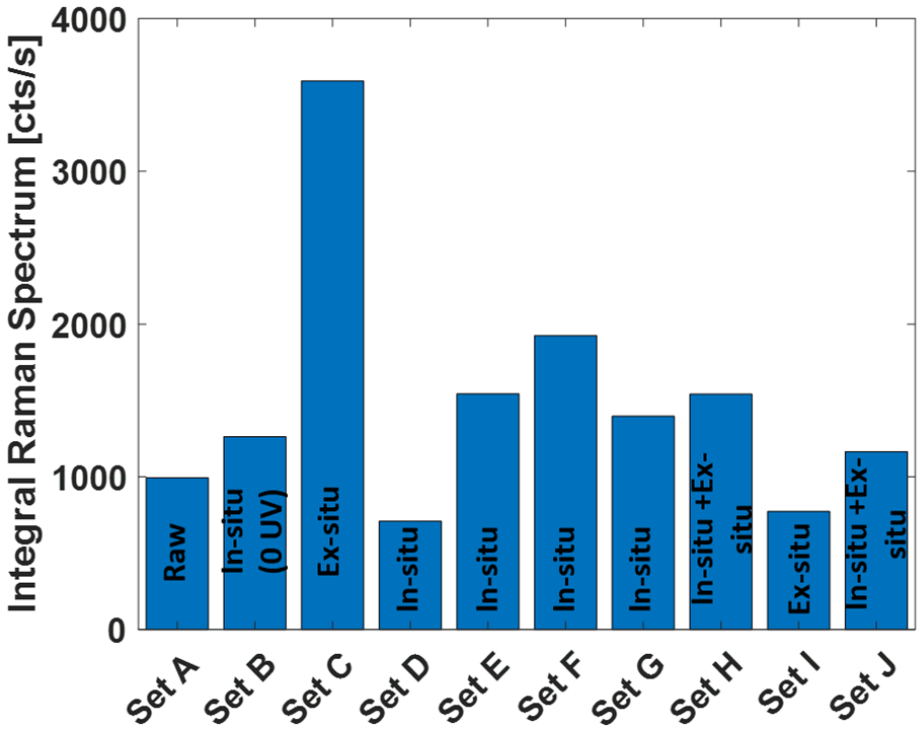

Figure 4.7: Comparison of integral spectral intensity from SERS spectra of Sets A, B, C, D, E, F, G, H, I, and J.

Figure 4.7 shows that the Raman signal enhancement for Set I (ex-situ integration) and Set J (ex-situ and in-situ integration) were lower when compared with Set C (exsitu integration) and Set H (ex-situ and in-situ integration) respectively. Different Raman integral in the result for different set of samples even when the same

conditions were applied suggests that inhomogeneous feature of tissue samples contribute to changing the SERS outcome even if the same conditions are applied.

4.7.2 Raman band assignment of SERS spectra obtained from shoulder tissue

Raman band assignment was performed in SERS spectrum from Set F (tissue samples with in-situ formation of gold nanoparticles at 20 mW) as shown in Figure 4.8 to better understand the tissue structure. It also confirmed that molecular fingerprints of tissue components can be observed when SERS is applied on the shoulder tissue samples. Figure 4.8 shows Raman bands from 820 cm^{-1} to 880 cm^{-1} which are responsible for C-C collagen bond [62]. Collagen is the dominant molecular compound for this type of musculoskeletal tissues. Other distinct peaks in the spectrum are identified as C-C stretch, α- helix from hydroxyproline of collagen (at 938 cm^{-1}), and the tissue minerals CO (at 1070 cm^{-1}) and PO (at 958 cm^{-1}) [62].

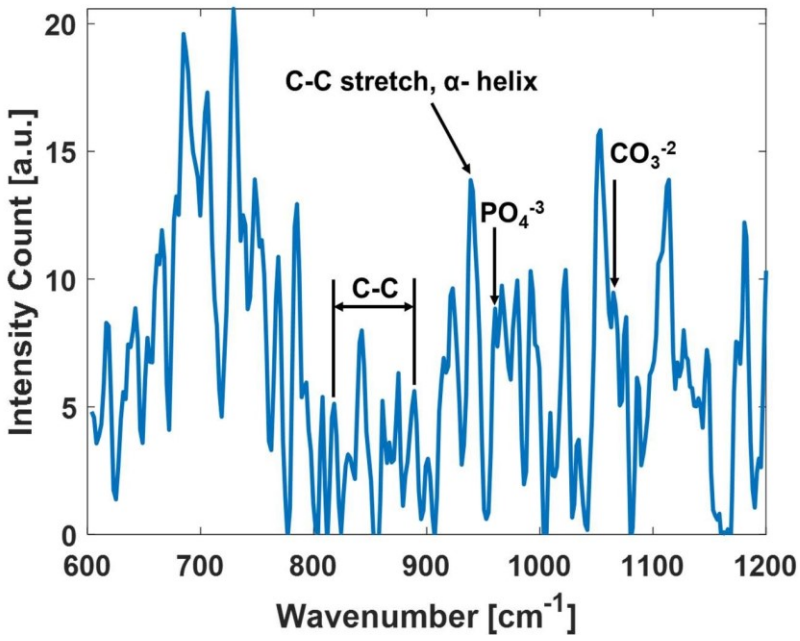

Figure 4.8: Raman band assignment in the SERS spectrum obtained set F.

This band assignment further proves that the experiment was successful in generating in-situ gold nanoparticles in tissue samples through UV photoreduction.

4.7.3 Raman signal in scanned image of shoulder tissue

As Figure 4.7 shows, the Raman signal intensity for different tissue samples can differ even when the conditions for preparing those samples are the same. Such a result is not unexpected. As tissues are combinations of different types of cells and bio substances, there is large variance in the cell environment of this type of bio samples. As a result, all slides will not produce the same quantity or quality of nanoparticles. To confirm this variance in tissue sample, scanning microscope components were integrated to the SERS experimental setup as shown in Figure 4.1 of section 4.3. The variance in a section of tissue sample and the extent to which this variation affects the SERS outcome is depicted in Figure 4.9 generated from the scanned image of SERS spectra.

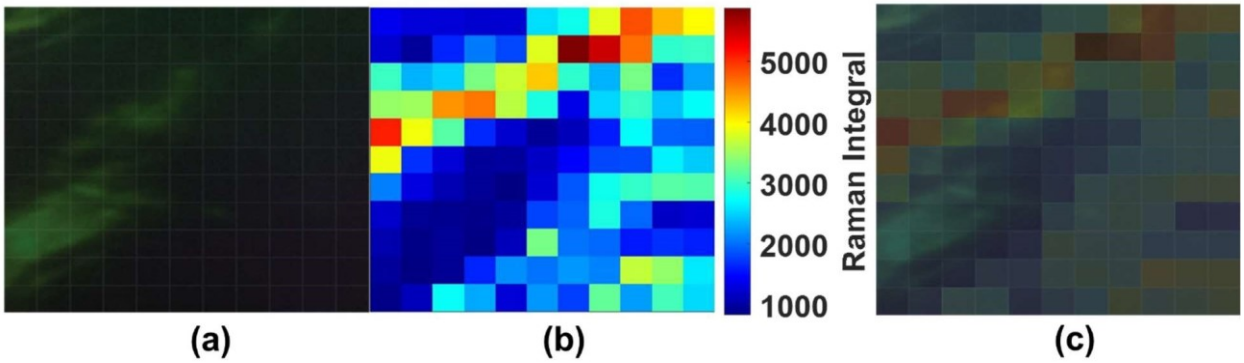

Figure 4.9: (a) Bright-field image of the scanned region of tissue sample, (b) scanned image of SERS spectra, and (c) image registration of bright field image and scanned image of SERS spectra obtained from the tissue sample.

As observed in Figure 4.2, the regions where in-situ gold nanoparticle generation was successful turned black. This phenomenon is also clearly observable from the bright-field image in Figure 4.9(a). The mapping image of SERS spectrum in Figure

4.9(b) showing Raman integral intensity with colours clearly demonstrates that even though gold nanoparticles were seen generated in the tissue samples and provided SERS spectrum, the quantity and quality of nanoparticles generated in each pixel of the image are not consistent throughout the image. As a result, large variation is observed in even a small region of the tissue sample, as shown in Figure 4.9(c).

To understand if any specific component of shoulder tissue affects gold nanoparticle integration and the resultant SERS signal, the colour bar of Raman integral intensity in Figure 4.9(b) was divided into 10 sections. The averaged Raman spectra of each section were then compared with other sections to understand the trend of increment in Raman integral intensity with tissue variance (as shown in Figure 4.10).

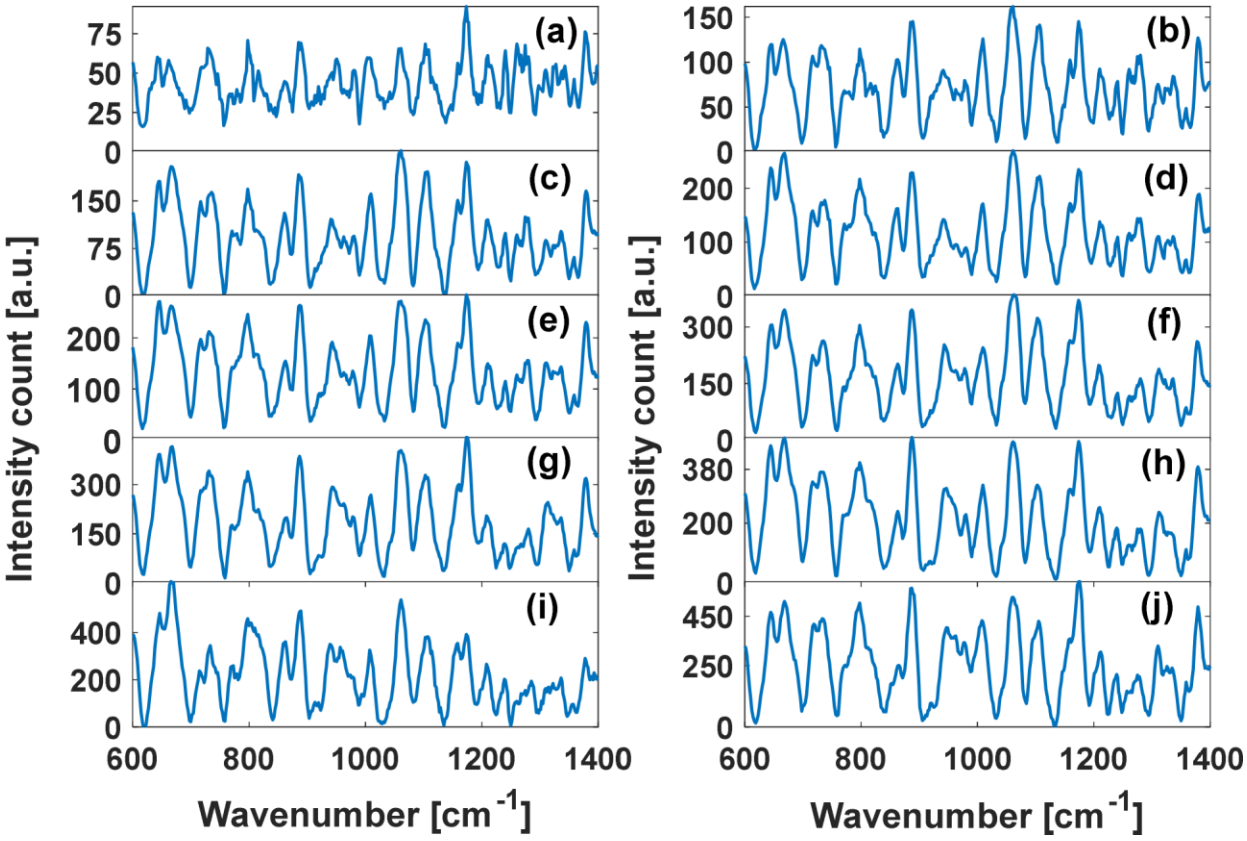

Figure 4.10: Raman spectra for Raman integral band (a) 833 to 1337, (b) 1337 to 1841, (c) 1841 to 2345, (d) 2345 to 2848, (e) 2848 to 3352, (f) 3352 to 3856, (g) 3856 to 4360, (h) 4360 to 4864, (i) 4864 to 5367, and (j) 5367 to 5871.

Table 6 shows the Raman band assignment of increasing peaks and the dominant peaks in each section of Raman integral band [62, 63, 64].

Table 6: Raman band assignment of 10 sections of the Raman integral colour bar on the scanned image of SERS spectra in Figure 4.9.

Raman integral bands based on colour bar in Figure 4.9	**Corresponding Raman bands showing increase in intensities with the increase in Raman integral band (cm^{-1})**	**Assignment**
833 to 1337	1170 (dominant peak)	Amide III
1337 to 1841	650-670	Monosodium Urate
	820-889	C-C collagen bond, Proline, Hydroxyproline
	1009	Type I collagen, Phenylalanine (Protein)
	1061	Proteoglycan (Protein)
	1107	Ring associated carbohydrate bond, isomer conformation in lipids
	1174	Amide III (peptide bond)
	1280	Amide III (peptide bond)

1841 to 2345	Same as previous Raman integral band	Same as previous Raman integral band
2345 to 2848	Same as previous Raman integral band	Same as previous Raman integral band
2848 to 3352	Same as previous Raman integral band	Same as previous Raman integral band
3352 to 3856	Same as previous Raman integral band	Same as previous Raman integral band
3856 to 4360	Same as previous Raman integral band	Same as previous Raman integral band
4360 to 4864	Same as previous Raman integral band	Same as previous Raman integral band
4864 to 5367	650-670 is dominant and other peaks same as previous Raman integral band	Same as previous Raman integral band (Monosodium Urate dominant)
5367 to 5871	Same as previous Raman integral band	Same as previous Raman integral band

The Raman integral is the lowest (833 to 1337) for the region where peptide bond-Amide III (at 1170 cm^{-1}) is dominant among other building components of shoulder tissue. This is expected because the sample attached to the glass slide has a coat of polylysine and this polymer compound is a chain of linear polypeptide with free amine side arms [65]. As a result, the dominant peak of Amide III in the lowest Raman integral range is observable. As the presence of different collagen

components (e.g., C-C collagen bond, proline, hydroxyproline, type I collagen), multiple protein components (e.g., phenylalanine, proteoglycan), carbohydrate bonds, and lipids increases, the Raman integral intensity increases, which suggests that these regions have high potential in generating the large quantity and good quality of gold nanoparticles required to enhance the Raman signal. However, band assignment on Raman spectrum from Raman integral band 4864 to 5367 shows that the dominant peak in that region comes from purines related to DNA/RNA [63, 64]. This reveals that the specific region of Raman integral band in the tissue slide had a large amount of purines deposition compared with other building components.

Most of the peaks in Raman spectra can be associated to multiple collagen and protein bands. This suggests that the presence of collagen and proteins are high in the region of tissue sample shown in the bright-field image of Figure 4.10. Moreover, it points that the regions of tissue enriched with collagen and different proteins have a high probability of generating a large number of good quality gold nanoparticles.

4.8 Discussion and conclusions

Data acquisition and final comparison presented in Figures 4.7 and 4.9 identify that the optimum condition selection for the tissue samples is not feasible without scanning the tissue sample. This means that to confirm the optimum condition needed for integration of gold nanoparticles to the tissue samples, further in-depth study of SERS spectra is required for each selected condition in Table 4 using Raman band assignment. Raman band assignment can assist to deliberate the effects of different conditions in SERS signal generation from the shoulder tissue samples. Moreover, it can help to overcome the inconsistency of SERS signal due to the variance in tissue sample. This can be achieved after spectral image scanning. Spectra with high Raman integrals can be sorted out and averaged from the scanned

spectral image (as shown in Figure 4.9(b)) for Raman band assignment. These outcomes for each set of selected conditions in Table 4 can be obtained and compared with each other to finalize the optimum condition for the clearest SERS outcomes of shoulder tissue samples. This optimization of SERS method application on shoulder tissue samples can lead us forward to a novel approach to diagnose PJI.

Chapter 5 Summary and future work

5.1 Summary

SERS is a powerful tool in biomolecule detection due to its high sensitivity and specificity. This thesis focuses on the detection of bacteria in two different biomedical applications using SERS. The first study focused on the optimization of capping agents for SERS detection of bacteria in human body while the second focused on developing a SERS method to detect shoulder tissue infections.

In the first application, three capping agents — polyvinylpyrrolidone (PVP), thioglucose, and citrate — were applied on the gold nanoparticles to analyze their effect in SERS detection of three different species of bacteria and identification of two strains of S. aureus. TG and citrate showed the best response in species detection of the bacteria, and thioglucose was the best among the three in the two-strain discrimination for S. aureus.

In the second application, ex-situ and in-situ methods of gold nanoparticle synthesis were applied on shoulder tissue samples to study the SERS outcome from shoulder tissue samples. This study showed that the application of SERS in shoulder tissue is possible and that in-situ generation of gold nanoparticles by UV exposure in tissue samples is also a successful approach. However, the optimum condition for SERS method remained unidentified due to the high variance in the tissue samples. This required integration of scanning microscope to the SERS setup used for the experiment. The scanned image of SERS spectra and its Raman band assignment confirmed the inhomogeneity in tissue sample causes inconsistent SERS spectra from one sample to the other even with same conditions applied. It is now understood that to overcome the tissue variance and decide the optimum SERS condition, scanning microscope involved SERS setup should be applied for each selected

conditions applied on the tissue samples. This can allow to collect the highest Raman integral spectra in each case and neglect low intensity Raman spectra following the Raman band assignment in each scenario to better understand the mechanism of SERS in shoulder tissue application.

5.2 Future work

5.2.1 Application of TG capped gold nanoparticles in SERS detection of bacteria

It is successfully demonstrated that E.coli, C.acnes and MRSA, MSSA strains of S.aureus can be successfully identified with 3 different capping agents (citrate, thioglucose and PVP) where citrate and thioglucose, both showed similar contribution in species detection and thioglucose showed the best response in strains identification of S.aureus. All bacteria species and strains utilized in this experiment for species and strain identification were in Lysogeny broth (LB) media. Since TG capped gold nanoparticles already showed outstanding response among the three capping in SERS identification of bacteria in this thesis, they are now utilized in our lab for species and strain identification of bacteria from serum and synovial fluid. Based on the outcomes from the serum and synovial media, the future target is to apply the thioglucose capped gold nanoparticles on the real patient samples for pathogen detection.

5.2.2 PJI diagnosis by SERS

PJI infection is caused by pathogens which are difficult to diagnose. Since SERS is a potential technique with high sensitivity and molecular specificity, it is selected to investigate PJI infection in shoulder tissue. We have conducted the first study of both ex-situ SERS and in-situ SERS by UV exposed photochemical reaction on the shoulder tissue. Different UV powers and incubation time were implemented to

optimize the SERS method for shoulder tissue application. Results of the optimization were inconsistent due to the inhomogeneity of the tissue samples. To confirm this inhomogeneity, scanning microscope was integrated to the dark field SERS setup. Then the scanned image of the SERS spectra showed that Raman integral intensity variation is high in even a small region of tissue for the nonuniform tissue environment. The Raman band assignment then confirmed that the region with high collagen and protein intensity can provide stronger Raman signal. This project is still ongoing. To complete the SERS optimization for PJI diagnosis, scanned image of SERS spectra is now obtained for each selected conditions in this thesis. These SERS image spectra should be generated for all sets of slides and then analysed with Raman band assignment. This can allow to neglect low Raman intensity spectra and consider the high integral Raman intensity for comparison among the conditions. Once the optimum UV-power is identified, then the results from ex-situ, in-situ and combination of both conditions can be compared to identify the best approach to apply SERS on the shoulder tissue samples. Future goal for this SERS method optimization is to apply on infected shoulder tissue samples to identify the PJI pathogen.

References

1. R. Hunter, A. N. Sohi, Z. Khatoon, V. R. Berthiaume, E. I. Alarcon, M. Godin, and H. Anis, "Optofluidic label-free SERS platform for rapid bacteria detection in serum," Sensors and Actuators B: Chemical 300, 126907 (2019).
2. A. K. Adya, and E. Canetta, "Nanotechnology and its applications to animal biotechnology," in Animal Biotechnology, Second edition (Academic Press/Elsevier 2020) pp. 309–326.
3. C.V. Raman, "A new radiation" [Reproduced from Indian J. Phys., 1928, 2, 387–398], Current Science 74, 382–386 (1998).
4. I. R. Lewis and H. G. M. Edwards, Handbook of Raman Spectroscopy (Marcel Dekker Inc., New York, 2001).
5. R. W. Boyd, Nonlinear Optics (Elsevier, 2020), pp. 381–493.
6. E. L. Ru and P. Etchegoin, Principles of Surface-Enhanced Raman Spectroscopy and related plasmonic effects (Elsevier, 2009).
7. R. W. Boyd, Nonlinear Optics (Elsevier, 2020), pp. 137-202.
8. S. Y. Ding, E. M. You, Z. Q. Tian, and M. Moskovits, "Electromagnetic theories of surface-enhanced Raman spectroscopy," Chemical Society Reviews 46, 4042-4076 (2017).
9. R. Hunter, "Medical diagnostics with Surface Enhanced Raman Scattering", PhD thesis (School of Electrical Engineering and Computer Science, University of Ottawa, 2016).
10. Z. Starowicz, R. Wojnarowska-Nowak, P. Ozga and E. M. Sheregii, "The tuning of the plasmon resonance of the metal nanoparticles in terms of the SERS effect", Colloid and Polymer Science 296, 1029–1037, 2018.
11. M. Fleischman, P. Hendra, and A. McQuillan, "Raman spectra of pyridine adsorbed at a silver electrode," Chemical Physics Letters 26, 163-166, (1974).

12. P. A. Mosier-Boss, “Review on SERS of Bacteria,” Biosensors (Basel) 7(4), 51, (2017).
13. D. L. Jeanmaire and R. P. Van Duyne, “Surface Raman spectroelectrochemistry. 1. Heterocyclic, aromatic, and aliphatic amines adsorbed on anodized silver electrode”, Journal of Electroanalytical Chemistry 84, 1–20 (1977).
14. M. G. Albrecht and J. A. Creighton, “Anomalously intense Raman spectra of pyridine at a silver electrode”, Journal of the American Chemical Society 99, 5215–5217 (1977).
15. A. Khetani, “Photonic crystal fiber as a robust Raman sensor,” PhD thesis (School of Electrical Engineering and Computer Science, University of Ottawa, 2016).
16. J. A. Sánchez-Gil, J. V. García-Ramos, and E. R. Mendez, “Electromagnetic mechanism in surface-enhanced Raman scattering from Gaussian-correlated randomly rough metal substrates,” Optics Express 10, 879–886 (2002).
17. A. Sadrolhosseini, A. Noor, and M. Moksin, “Application of surface plasmon resonance based on a metal nanoparticle,” in Plasmonics — Principles and Applications, K. Y. Kim, ed. (IntechOpen, 2012), pp. 253–282.
18. N. D. Israelsen, C. Hanson, and E. Vargis, “Nanoparticle properties and synthesis effects on surface-enhanced Raman scattering enhancement factor: An introduction,” The Scientific World Journal 2015, 1–12 (2015).
19. R. Pilot, R. Signorini, C. Durante, L. Orian, M. Bhamidipati, and L. Fabris, “A Review on Surface-Enhanced Raman Scattering,” Biosensors 9(2), 57 (2019).
20. R. A. Tripp, R. A. Dluhy, and Y. Zhao, “Novel nanostructures for SERS biosensing,” NanoToday 3, 31–37 (2008).

21. K. C. Bantz, A. F. Meyer, N. J. Wittenburg, H. Im, Ö. Kurtulus, S. H. Lee, N. C. Lindquist, S.-H. Oh, and C. L. Haynes, “Recent Progress in SERS Biosensing”, Physical chemistry chemical physics 13, 11551–11567 (2011).
22. G. Papadakis, P. Murasova, A. Hamiot, K. Tsougeni, G. Kaprou, M. Eck, D. Rabus, Z. Bilkova, B. Dupuy, G. Jobst, A. Tserepi, E. Gogolides, E. Gizeli, “Micro-nano-bio acoustic system for the detection of foodborne pathogens in real samples,” Biosens Bioelectron 111, 52–58 (2018).
23. K.S. Gracias, J.L. McKillip, “A review of conventional detection and enumeration methods for pathogenic bacteria in food”, Can. J. Microbiol. 50 883–890 (2004).
24. Y. Yamamoto, “PCR in Diagnosis of Infection: Detection of bacteria in cerebrospinal fluids”, Clin. Vaccine Immunol. 9 508–514 (2002).
25. E. Carbonnelle, C. Mesquita, E. Bille, N. Day, B. Dauphin, J.-L. Beretti, A. Ferroni, L. Gutmann, X. Nassif, “MALDI-TOF mass spectrometry tools for bacterial identification in clinical microbiology laboratory”, Clin. Biochem. 44 104–109 (2011).
26. F. Molina, E. López-Acedo, R. Tabla, I. Roa, A. Gómez, J.E. Rebollo, “Improved detection of Escherichia coli and coliform bacteria by multiplex PCR”, BMC Biotechnol. 15 48 (2015).
27. P. R. West, S. Ishii, G. V. Naik, N. K. Emani, V. M. Shalaev, and A. Boltasseva, “Searching for better plasmonic materials,” Laser and Photonics Reviews 4, 795–808 (2010).
28. C. M. Phan and H. M. Nguyen, “Role of capping agent in wet synthesis of nanoparticles,” The Journal of Physical Chemistry A 121, 3213–3219 (April 11, 2017).

29. B. Ajitha, Y. A. K. Reddy, P. S. Reddy, H.-J. Jeon, and C. W. Ahn, “Role of capping agents in controlling silver nanoparticles size, antibacterial activity and potential application as optical hydrogen peroxide sensor,” Royal Society of Chemistry 6, 32171–36179 (2016).
30. Y. N. Slavin, J. Asnis, U. O. Häfeli, and H. Bach, “Metal nanoparticles: understanding the mechanisms behind antibacterial activity,” Journal of Nanobiotechnology 15(65), (2017).
31. Y. Nur, “Gold nanoparticles: synthesis, characterisation and their effect on Pseudomonas flourescens,” PhD thesis (School of Geography, Earth and Environmental Sciences, University of Birmingham, 2013).
32. F. Porcaro, L. Carlini, A. Ugolini, D. Visaggio, P. Visca, I. Fratoddi, I. Venditti, C. Meneghini, L. Simonelli, C. Marini, W. Olszewski, N. Ramanan, I. Luisetto, and C. Battocchio, “Synthesis and structural characterization of silver nanoparticles stabilized with 3-mercapto-1-propansulfonate and 1thioglucose mixed thiols for antibacterial applications,” Materials 9(12), (December 2016).
33. J. Dong, P. L. Carpinone, G. Pyrgiotakis, P. Demokritou, and B. M. Moudgil, Synthesis of Precision Gold Nanoparticles Using Turkevich Method, KONA Powder and Particle Journal, August 24, 2019.
34. A. Rostek, D. Mahl, M. Epple, “Chemical composition of surface-functionalized gold nanoparticles”, J Nanopart Res 13:4809–4814 (2011).
35. W. Wang, X. Ding, Q. Xu, J. Wang, L. Wang, and X. Lou, “Zeta-potential data reliability of gold nanoparticle biomolecular conjugates and its application in sensitive quantification of surface absorbed protein”, Colloids and Surfaces B: Biointerfaces, 148, 541-548 (2016).

36. E. Joseph and G. Singhvi, “Multifunctional nanocrystals for cancer therapy: a potential nanocarrier”, Nanomaterials for Drug Delivery and Therapy, 2019.
37. T. Zheng, S. Bott, and Q. Huo, “Techniques for accurate sizing of gold nanoparticles using dynamic light scattering with particular application to chemical and biological sensing based on aggregate formation”, ACS Applied Materials and Interfaces, 8, 21585-21594 (2016).
38. V. Amendola and M. Meneghetti, “Size Evaluation of Gold Nanoparticles by UV-vis Spectroscopy”, The Journal of Physical Chemistry C, 113, 4277–4285, (2009).
39. S. Link and M. A. El-Sayed, “Shape and size dependence of radiative, non-radiative and photothermal properties of gold nanocrystals,” International Reviews in Physical Chemistry, 19, 409–453 (2000).
40. L. M. Payne, W. Langbein, and P. Borri, “Polarization-resolved extinction and scattering cross-section of individual gold nanoparticles measured by wide-field microscopy on a large ensemble,” Applied Physics Letters 102, 131107 (January 2013).
41. Z.-M. Zhang, S. Chen, and Y.-Z. Liang, “Baseline correction using adaptive iteratively reweighted penalized least squares,” Analyst 135, 1138–1146 (February 2010).
42. R. Hunter and H. Anis, “Genetic support vector machines as powerful tools for the analysis of biomedical Raman spectra,” Journal of Raman Spectroscopy, 49, 1435–1444 (2018).
43. D. K. Duvenaud, “Automatic model construction with Gaussian processes,” PhD thesis (Cambridge University, 2014).
44. L. C. Lee, C.-Y. Liong and A. A. Jemain, “Partial Least Squares-Discriminant Analysis (PLS-DA) for Classification of high-dimensional (HD) data: a

review of contemporary practice strategies and knowledge gaps", Royal Society of Physical Chemistry, 00, 1-3, 2012.

45. S. R. Smith, R. Seenath, M. R. Kulak, and J. Lipkowski, "Characterization of a self-assembled monolayer of 1-thioβ-D-glucose with electrochemical surface enhanced Raman spectroscopy using a nanoparticle modified gold electrode," Langmuir 31, 10076−10086 (2015).
46. A. Kedia, and P. S. Kumar, "Solvent-adaptable poly(vinylpyrrolidone) binding induced anisotropic shape control of gold nanostructures," The Journal of Physical Chemistry C 116, 23721−23728 (2012).
47. M. Rani, L. Moudgil, B. Singh, A. Kaushal, A. Mittal, G. S. S. Saini, S. K. Tripathi, G. Singh, and A. Kaura, "Understanding the mechanism of replacement of citrate from the surface of gold nanoparticles by amino acids: A theoretical and experimental investigation and their biological application," RSC Advances 6, 17373–17383 (February 1, 2016).
48. M. Chisanga, H. Muhamadali, D. I. Ellis, and R. Goodacre, "Surface-enhanced Raman scattering (SERS) in microbiology: Illumination and enhancement of the microbial world," Applied Spectroscopy 72, 987–1000 (2018).
49. P. Hildebrandt and S. Lecomte, "Biochemical applications of Raman spectroscopy," in Encyclopedia of Spectroscopy and Spectrometry, J. C. Lindon, G. E. Tranter, and J. L. Holmes, eds. (Academic Press, 1999) pp. 88–97.
50. T. -Y. Chan, T. -Y. Liu, K. -S. Wang, K. -T. Tsai, Z. -X. Chen, Y. -C. Chang, Y. -Q. Tseng, C. -H. Wang, J. -K. Wang, and Y. -L. Wang, "SERS Detection of Biomolecules by Highly Sensitive and Reproducible Raman Enhancing Nanoparticle Array", Nanoscale Research Letters, 12, 344 (2017).

51. B. Fink and F. Sevelda, “Periprosthetic Joint Infection of Shoulder Arthroplasties: Diagnostic and Treatment Options,” BioMed Research International 2017, Article ID 4582756 (2017).
52. J. Richards, M. C. S. Inacio, M. Beckett, et al., “Patient and procedure-specific risk factors for deep infection after primary shoulder arthroplasty,” Clinical Orthopaedics and Related Research 472, 2809–2815 (2014).
53. P. Pottinger, S. Butler-Wu, M. B. Neradilek, et al., “Prognostic factors for bacterial cultures positive for Propionibacterium acnes and other organisms in a large series of revision shoulder arthroplasties performed for stiffness, pain, or loosening,” Journal of Bone & Joint Surgery 94, 2075–2083 (2012).
54. K. E. Piper, M. J. Jacobson, R. H. Cofield, et al., “Microbiologic diagnosis of prosthetic shoulder infection by use of implant sonication,” Journal of Clinical Microbiology 47, 1878–1884 (2009).
55. S. Sun, P. Mendes, K. Critchley, S. Diegoli, M. Hanwell, S. D. Evans, G. J. Leggett, J. A. Preece, and T. H. Richardson, “Fabrication of Gold Micro- and Nanostructures by Photolithographic Exposure of Thiol-Stabilized Gold Nanoparticles”, Nano Letters, 6, 345-350 (2006).
56. J. Polte, R. Erler, A.F. Thunemann, S. Sokolov, T. T. Ahner, K. Rademann, F. Emmerling, and R. Kraehnert, “Nucleation and growth of gold nanoparticles studied via in situ small angle X-ray sScattering at millisecond time resolution,” ACS Nano 4, 1076–1082 (2010).
57. K. Liu, Z. He, J. F. Curtin, H. J. Byrne, and F. Tian, “A novel, rapid, seedless, in situ synthesis method of shape and size controllable gold nanoparticles using phosphates,” Scientific Reports 9 (2019).

58. M. Abbas, H.H. Susapto, and C.A.E. Hauser, “Synthesis and organization of gold-peptide nanoparticles for catalytic activities,” ACS Omega 7, 2082–2090 (2022).
59. N. Jara, N. S. Milán, A. Rahman, L. Mouheb, D. C. Boffito, C. Jeffryes, and S. A. Dahoumane, “Photochemical synthesis of gold and silver nanoparticles — A review,” Molecules 26, 4585 (2021).
60. S. Hong, “Optimization, Modification and Application of Gold Nanoparticles as the Substrates of Surface Enhanced Raman Spectroscopy,” PhD thesis (Department of Chemistry, University of South Florida, 2013).
61. M. Sengani, A. M. Grumezescu, and V. D. Rajeswari, “Recent trends and methodologies in gold nanoparticle synthesis — A prospective review on drug delivery aspect,” Open Nano 2, 37–46 (2017).
62. K. Esmonde-White, “Raman spectroscopy of soft musculoskeletal tissues,” Applied Spectroscopy OA 68, 1203–1218 (2014).
63. M. Fosca, V. Basoli, E. D. Bella, F. Russo, G. Vadalà, M. Alini, J. V. Rau, and S. Verrier, “Raman spectroscopy in skeletal tissue disorders and tissue engineering: present and prospective,” Tissue Engineering Part B: Reviews (January 2022).
64. O. A. Azher, “Spectroscopic Characterisation of Purine Nucleotides and their Interaction with Proteins,” PhD thesis (Faculty of Science and Engineering, University of Manchester, 2018).
65. D. Kasala, C. -O. Yun, “Polymer-Anchored Adenovirus as a Therapeutic Agent for Cancer Gene Therapy”, Adenoviral Vectors for Gene Therapy (Second Edition), 29, 707-737 (2016).